TWO SMALL TEMPERATE PLANETS TRANSITING NEARBY M DWARFS IN *K*2 CAMPAIGNS 0 AND 1[*][†][‡]

JOSHUA E. SCHLIEDER[1,16,17], IAN J. M. CROSSFIELD[2,18], ERIK A. PETIGURA[3,19], ANDREW W. HOWARD[4], KIMBERLY M. ALLER[4,17],
EVAN SINUKOFF[4], HOWARD T. ISAACSON[5], BENJAMIN J. FULTON[4], DAVID R. CIARDI[6], MICKAËL BONNEFOY[7], CARL ZIEGLER[8],
TIMOTHY D. MORTON[9], SÉBASTIEN LÉPINE[10], CHRISTIAN OBERMEIER[11], MICHAEL C. LIU[4], VANESSA P. BAILEY[12],
CHRISTOPH BARANEC[13], CHARLES A. BEICHMAN[6], DENIS DEFRÈRE[14], THOMAS HENNING[11], PHILIP HINZ[14],
NICHOLAS LAW[8], REED RIDDLE[3], AND ANDREW SKEMER[14,15,19]

[1] NASA Ames Research Center, Space Science and Astrobiology Division, MS 245-6, Moffett Field, CA 94035, USA; joshua.e.schlieder@nasa.gov
[2] Lunar & Planetary Laboratory, University of Arizona, 1629 E. University Blvd., Tucson, AZ, USA
[3] California Institute of Technology, Pasadena, CA 91125, USA
[4] Institute for Astronomy, University of Hawai'i, 2680 Woodlawn Drive, Honolulu, HI, USA
[5] Astronomy Department, University of California, Berkeley, CA, USA
[6] NASA Exoplanet Science Institute, California Institute of Technology, 770 S. Wilson Ave., Pasadena, CA 91125, USA
[7] Université Grenoble Alpes, IPAG, 38000, Grenoble, 38000, Grenoble; CNRS, IPAG, F-38000 Grenoble, France
[8] University of North Carolina at Chapel Hill, Chapel Hill, NC 27599, USA
[9] Department of Astrophysics, Princeton University, Princeton NJ 08544, USA
[10] Department of Physics & Astronomy, Georgia State University, Atlanta, GA, USA
[11] Max-Planck-Institut für Astronomie, Königstuhl 17, D-69117, Heidelberg, Germany
[12] Kavli Institute for Particle Astrophysics and Cosmology, Stanford University, Stanford, CA 94305, USA
[13] Institute for Astronomy, University of Hawai'i at Mānoa, Hilo, HI 96720-2700, USA
[14] Steward Observatory, Department of Astronomy, University of Arizona, 933 N. Cherry Ave, Tucson, AZ 85721, USA
[15] Department of Astronomy and Astrophysics, University of California, Santa Cruz, CA 95064, USA

ABSTRACT

The prime *Kepler* mission revealed that small planets ($<4\ R_\oplus$) are common, especially around low-mass M dwarfs. *K*2, the repurposed *Kepler* mission, continues this exploration of small planets around small stars. Here we combine *K*2 photometry with spectroscopy, adaptive optics imaging, and archival survey images to analyze two small planets orbiting the nearby field-age M dwarfs, K2-26 (EPIC 202083828) and K2-9. K2-26 is an M1.0 $\pm$ 0.5 dwarf at 93 $\pm$ 7 pc from *K*2 Campaign 0. We validate its planet with a day period of 14.5665 and estimate a radius of $2.67^{+0.46}_{-0.42}\ R_\oplus$. K2-9 is an M2.5 $\pm$ 0.5 dwarf at 110 $\pm$ 12 pc from *K*2 Campaign 1. K2-9b was first identified by Montet et al.; here we present spectra and adaptive optics imaging of the host star and independently validate and characterize the planet. Our analyses indicate K2-9b is a $2.25^{+0.53}_{-0.96}\ R_\oplus$ planet with a 18.4498 day period. K2-26b exhibits a transit duration that is too long to be consistent with a circular orbit given its measured stellar radius. Thus, the long transits are likely due to the photoeccentric effect and our transit fits hint at an eccentric orbit. Both planets receive low incident flux from their host stars and have estimated equilibrium temperatures <500 K. K2-9b may receive approximately Earth-like insolation. However, its host star exhibits strong *GALEX* UV emission which could affect any atmosphere it harbors. K2-26b and K2-9b are representatives of a poorly studied class of small planets with cool temperatures that have radii intermediate to Earth and Neptune. Future study of these systems can provide key insight into trends in bulk composition and atmospheric properties at the transition from silicate dominated to volatile rich bodies.

Key words: eclipses – stars: individual (K2-26, K2-9) – techniques: photometric – techniques: spectroscopic

1. INTRODUCTION

Planets are commonplace in the Galaxy. In the last 20 years, knowledge of planet demographics, architectures, and frequencies has expanded beyond the eight primary bodies in our solar system to thousands of planets orbiting thousands of stars. A workhorse of this exoplanet revolution is the *Kepler* space telescope. Transit data collected during the prime mission of *Kepler* revealed that small planets—Earth analogues, super-Earths, and sub-Neptunes ($R_p < 4\ R_\oplus$)—are abundant around Sun-like stars (Petigura et al. 2013a). Statistical studies focusing on the few M dwarfs ($T_{\rm eff} \lesssim 4000$ K, $M_* \lesssim 0.6\ M_\odot$) that *Kepler* observed (3900 stars) revealed that small planets exist around *nearly all* M dwarfs (Dressing & Charbonneau 2013, 2015).

The small radii and masses of M dwarfs combined with their sheer numbers (~70% of all stars, Bochanski et al. 2010) provide the best opportunities to detect and characterize small planets in the Solar neighborhood. Because of the large

numbers of M dwarfs and the high frequency of planets around them, the closest Earth-size planets in the habitable zone almost certainly orbit these low-mass stars. Planets of a given radius transiting M dwarfs exhibit deeper transit signatures and planets of a given mass produce larger stellar reflex motions (Howard et al. 2012). Additionally, the atmospheres of small planets orbiting M dwarfs are more amenable to transmission spectroscopy studies (e.g., Kreidberg et al. 2014) due to the favorable star-to-planet radius ratio. However, since *Kepler* observed relatively few of these stars, the number of small planets detected and validated in transit around M dwarfs remains small. Subsequently, their demographics, formation scenarios, and the evolution of their orbits remain poorly constrained.

We are pursuing a program to identify and characterize additional small planets transiting M dwarfs using data from *K*2, the 2 reaction wheel, ecliptic plane survey of NASA's repurposed *Kepler* spacecraft (Howell et al. 2014). The *K*2 M Dwarf Program (*K*2-MDP) is a comprehensive approach to select M dwarf targets in each *K*2 field, generate calibrated light curves, identify candidate transiting planets, and obtain followup observations to validate and characterize the planetary systems. The first discoveries from the *K*2-MDP are K2-3 and K2-21, M0 dwarfs within 100 pc, each hosting multiple transiting super-Earths (Crossfield et al. 2015; Petigura et al. 2015). K2-3bcd, K2-21bc, and other early *K*2 discoveries (Montet et al. 2015; Vanderburg et al. 2015) have provided planets that occupy poorly explored regions of the planetary mass–radius– temperature diagram ($R_p < 4\,R_\oplus$, $T_{eq} < 600$ K), some ideal early targets for spectroscopic followup with the *James Webb Space Telescope* (*JWST*, Beichman et al. 2014; Batalha et al. 2015), and some truly novel systems (i.e., WASP-47bcd, Becker et al. 2015), all well before the launch of the *Transiting Exoplanet Survey Satellite* (*TESS*, Ricker et al. 2014).

Here we present the discovery and validation of a small cool planet orbiting the nearby M dwarf, K2-26, and an independent validation and detailed characterization of the known planet transiting the M dwarf K2-9. In Section 2 we describe the observations of these systems using *K*2 and ground-based spectroscopy and imaging. We detail our analyses of these observed data and the results in Section 3. Section 4 provides a discussion of the properties of these planets in the context of known demographics and Section 5 provides concluding remarks.

2. OBSERVATIONS AND DATA REDUCTION

2.1. K2 Target Selection, Photometry, and Transit Search

We identified the high proper motion stars PM I06168+2435 and PM I11450+0000 (LP 613–39, NLTT 28423) as candidate M dwarf targets for our *K*2 Campaign 0 (C0: GO0120—PI Lépine) and Campaign 1 (C1: GO1036—PI Crossfield) proposals, respectively. The stars were also proposed as targets in C0 and C1 by several other groups (C0: GO0111—PI Sanchis Ojeda, GO0119—PI Montet; C1: GO1052—PI Robertson, GO1053—PI Montet, GO1059—PI Stello, GO1062—PI Anglada-Escudé). We selected these targets as candidate nearby M dwarfs from the SUPERBLINK proper motion survey (Lépine & Shara 2005; Lépine & Gaidos 2011) following the photometric and proper motion criteria described in Crossfield et al. (2015). A coordinate cross-match of PM I06168 + 2435 and PM I11450 + 0000 with the *K*2 *Ecliptic*

Table 1
Summary of Stellar Properties

Parameter	K2-26	K2-9	References
α (hh:mm:ss)	06:16:49.579	11:45:03.472	(1)
δ (dd:mm:ss)	+24:35:47.08	+00:00:19.08	(1)
μ_α (mas yr^{-1})	−27.8 ± 4.1	−171.6 ± 3.8	(2)
μ_δ (mas yr^{-1})	−117.9 ± 4.1	32.1 ± 3.8	(2)
RV (km s^{-1})	95.34 ± 0.15	−31.02 ± 0.15	(1)
d_{phot} (pc)	93 ± 7	110 ± 12	(1)
Kep (mag)	14.00	14.96	(1)
B(mag)	15.97 ± 0.13	...	(3)
V(mag)	14.53 ± 0.03	15.63[a]	(3)
B_{POSSI} (mag)	16.16	16.55	(2)
R_{POSSI} (mag)	13.14	14.41	(2)
g' (mag)	15.296 ± 0.023	16.652 ± 0.117	(3)
r' (mag)	13.927 ± 0.080	15.218 ± 0.018	(3)
i' (mag)	13.421 ± 0.493	14.147 ± 0.095	(3)
J (mag)	11.350 ± 0.024	12.451 ± 0.024	(4)
H (mag)	10.762 ± 0.022	11.710 ± 0.022	(4)
K_s (mag)	10.530 ± 0.018	11.495 ± 0.023	(4)
*W*1 (mag)	10.422 ± 0.023	11.348 ± 0.022	(5)
*W*2 (mag)	10.349 ± 0.021	11.214 ± 0.021	(5)
*W*3 (mag)	10.409 ± 0.086	11.354 ± 0.193	(5)
Spectral Type	M1.0V ± 0.5	M2.5V ± 0.5	(1)
T_{eff} (K)	3785 ± 185	3390 ± 150	(1)
[Fe/H] (dex)	−0.13 ± 0.15	−0.25 ± 0.20	(1)
Radius ($R_\odot$)	0.52 ± 0.08	0.31 ± 0.11	(1)
Mass ($M_\odot$)	0.56 ± 0.10	0.30 ± 0.14	(1)
Luminosity ($L_\odot$)	0.049 ± 0.023	0.012 ± 0.010	(1)
Density (g cm^{-3})	3.92 ± 1.43	9.88 ± 4.25	(1)
Age (Gyr)	$\gtrsim 1$	$\gtrsim 1$	(1)

Note.
[a] Estimated using photometric relations in Lépine & Shara (2005).
References. (1) This work, (2) Roeser et al. (2010, PPMXL), (3) Henden et al. (2012, APASS DR9), (4) Cutri et al. (2003, 2MASS), and (5) Cutri et al. (2013, ALLWISE).

Plane Input Catalog (EPIC) returned matches with the sources EPIC 202083828 and K2-9, respectively. K2-9 was given the *K*2 identifier K2-9 by NExScI[20] after validation of its planet in Montet et al. (2015). EPIC 202083828 was designated K2-26 after validation of its planet in Section 3.4 of this work. EPIC 202083828 was observed by *K*2 in long-cadence mode during C0 from 2014 March 08 to May 27 and K2-9 was observed using the same mode during C1 from 2014 May 30 to August 21. We provide basic identifying information and available photometry for these stars in Table 1.

The degraded pointing precision of *K*2 due to the loss of 2 reaction wheels leads to telescope drift in the form of a roll around the telescope boresight. This drift is corrected using thruster fires when the spacecraft reaches a predetermined roll limit approximately every 6 hr. The periodic drift and correction of a star over ∼1 pixel leads to systematic brightness variations of ∼0.5%. These variations are roll angle dependent and must be corrected in the light curve extraction process. Our approach to correcting these effects and extracting calibrated photometry from the raw *K*2 pixel data is identical to that described in Crossfield et al. (2015). In general we perform a frame-by-frame median flux subtraction and compute the the
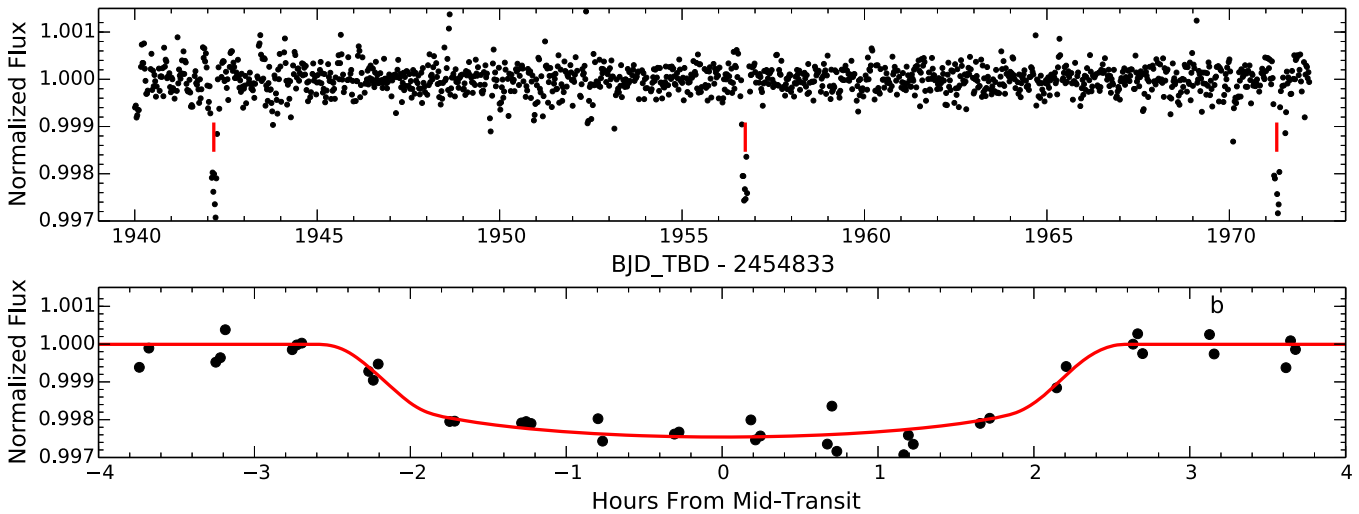

Figure 1. Top: calibrated *K*2 photometry for K2-26 (EPIC 202083828). Vertical ticks indicate the locations of the transits. Bottom: phase-folded photometry and best-fit light curve. The ~4.7 hr transit duration is likely the result of an eccentric orbit.
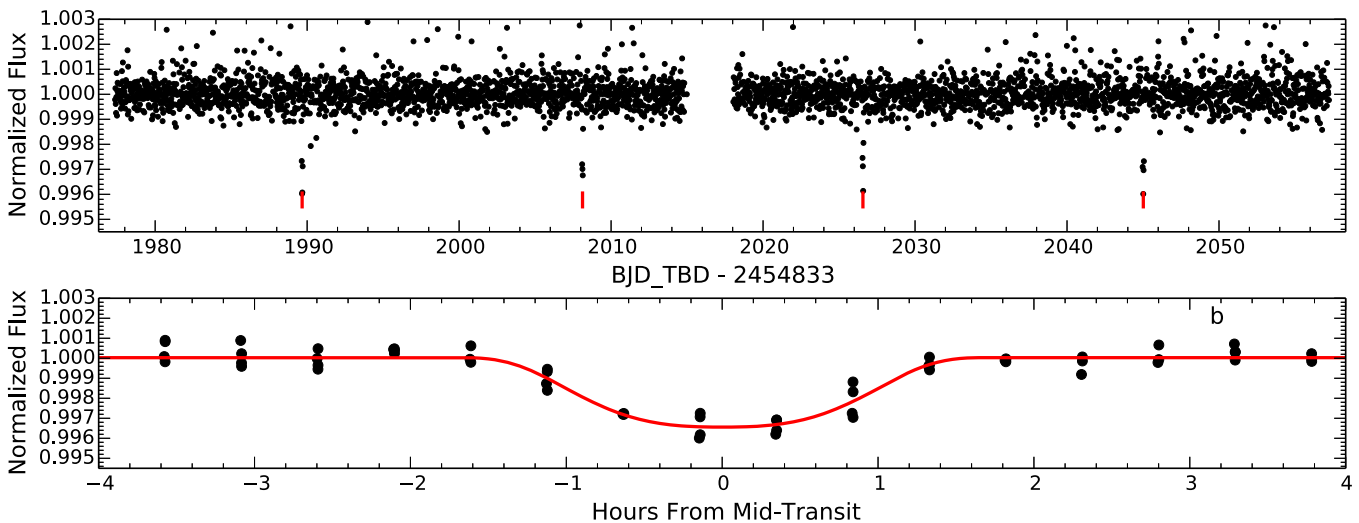

Figure 2. Top: calibrated *K*2 photometry for K2-9. Vertical ticks indicate the locations of the transits. Bottom: phase-folded photometry and best-fit light curve.

raw photometry by summing the single frame flux within a circular aperture centered on the target. We then compute the principal components of the row and column centroids and fit a Gaussian process (GP) to remove the systematic variations. In practice the GP fitting is iterative and updates are made to the GP parameters to minimize the rms fit residuals. The flux extraction and GP fitting procedures are repeated for apertures of varying sizes until an aperture size is found that minimizes the rms residuals in the calibrated light curve. The extraction apertures for K2-26 and K2-9 were soft-edged circular apertures having radii of 2 and 3 pixels, respectively. After correcting for spacecraft roll, both stars exhibited smooth, low-amplitude, slowly modulating, photometric variations on the order of 1%. These features could be related to intrinsic stellar variability or be unaccounted for spacecraft systematics, possibly the result of small focus changes due to thermal expansion and contraction over the course of a *K*2 observing campaign. If the observed residual variability is at least in part intrinsic to the stars, i.e., star spots, it is very low-level and indicative of slow rotation rates in both cases (~weeks). Prior to searching for transit events in the light curves, this residual

variability is also removed. The calibrated *K*2 light curves for the stars are shown in top panels of Figures 1 and 2 and are available upon request.

We searched the calibrated and detrended light curves of K2-26 and K2-9 using the TERRA algorithm, an automated, grid-based, transit search pipeline (Petigura & Marcy 2012; Petigura et al. 2013b). Our TERRA search of the K2-26 photometry identified a candidate planet with a period of $P \approx 14.567$ day and an S/N ≈ 34. A candidate was also detected transiting K2-9 with $P \approx 18.450$ day and S/N ≈ 24. Each of these transit signals was fit with a Mandel & Agol (2002) transit model which we show in the bottom panels of Figures 1 and 2. We then masked out the in-transit observations of each planet candidate and searched for additional transit signals with TERRA. This subsequent search of each light curve returned no further candidates above our signal-to-noise ratio (S/N) threshold of 12. We note that the maximum likelihood periods for the candidates transiting K2-26 and K2-9 are close to integer multiples of the observing cadence. We consider this a priori unlikely and hypothesize that residual systematics exist in the *K*2 photometry after our photometric processing. The *K*2

C0-C3 candidate catalog of Vanderburg et al. ([2016](#)) includes K2-26 and K2-9 with periods of 14.5670 day and 18.4487 day (no uncertainties), respectively. The Vanderburg et al. ([2016](#)) photometry was extracted using an independent analysis and they found periods consistent with ours at the $\sim 0.3\sigma$ and $\sim 0.8\sigma$ levels. Montet et al. ([2015](#)) also report an independent period for K2-9 of 18.44883 ± 0.00137 day, which is consistent with our estimate at the $\sim 1\sigma$ level. Thus, we conclude that any systematic errors that favor periods that are near-integer multiples of the $K2$ long cadence are second order and have minimal impact on our reported parameters. To validate and characterize these candidate planets, we obtain and analyze spectroscopic and imaging data, perform detailed checks of the $K2$ pixel level photometry and light curves, and estimate false positive probabilities (FPPs). These observations and analyses are described in the following sections.

2.2. Followup Spectroscopy

2.2.1. IRTF/SpeX

We observed K2-26 and K2-9 using the near-infrared cross-dispersed spectrograph (SpeX, Rayner et al. [2003](#)) on the 3.0 m NASA Infrared Telescope facility on 2015 May 02 UT and 2015 April 16 UT, respectively. K2-26 was observed under clear skies with an average seeing of $\sim 0\rlap{.}''6$. K2-9 was observed under poorer conditions with thin, variable cirrus, high humidity, and seeing between $1\rlap{.}''0-1\rlap{.}''2$. We used the instrument in short cross-dispersed mode using the $0.3 \times 15''$ slit which provides wavelength coverage from 0.68 to 2.5 μm at a resolution of $R \approx 2000$. The stars were dithered to two positions along the slit following an AB pattern for sky subtraction. The K2-26 observing sequence consisted of 8×75 s exposures for a total integration time of 600 s. K2-9 was observed for 24×120 s for a total time of 2880 s. We also observed an A0 standard and flat and arc lamp exposures immediately after each star for telluric correction and wavelength calibration.

The data were reduced using the SpeXTool package (Vacca et al. [2003](#); Cushing et al. [2004](#)). SpeXTool performs flat-fielding; bad pixel removal; wavelength calibration; sky subtraction; spectral extraction and combination; telluric correction; flux calibration; and order merging. The final calibrated spectra had S/N of ~ 80 per resolution element in the H- ($\sim 1.6\,\mu$m) and K-bands ($\sim 2.2\,\mu$m). The spectral quality decreases rapidly toward bluer wavelengths with S/N ~ 60 in the J-band ($\sim 1.25\,\mu$m) and ~ 10 at 0.75 μm. The JHK-band spectra are compared with late-type standards from the IRTF Spectral Library[21] (Cushing et al. [2005](#); Rayner et al. [2009](#)) in Figures [3](#) and [4](#). K2-26 is a best visual match to the M1 standard across the near-IR bands. K2-9 is later-type and matches well with the M2/M3 standards.

2.2.2. NTT/EFOSC2

On UT 2015 January 11, we observed K2-26 using the ESO Faint Object Spectrograph and Camera (v.2) (EFOSC2, Buzzoni et al. [1984](#)) mounted to the Nasmyth B focus of the 3.6 m ESO New Technology Telescope (NTT). These observations were made as part of our 70 night $K2$ followup program (PID 194.C-0443, PI: I.J.M. Crossfield). The star was observed under good conditions with average seeing $\sim 1\rlap{.}''0$ and

a total integration time of 270 s. We used EFOSC2 in spectroscopic mode with the $0\rlap{.}''3$ slit and grism 16 to provide a resolution of $R \sim 1600$ from 0.6 to 1.0 μm. We also obtained standard bias, flat, and HeAr lamp calibration frames immediately after observing K2-26 along with observations of spectrophotometric standards for flux calibration (Bohlin et al. [2001](#)).

The EFOSC2 data was reduced using standard IRAF[22] routines that included bias subtraction, flat-fielding, wavelength calibration, and spectral extraction. The spectrum was then flux calibrated using a standard observed close-in time. The final calibrated spectrum had an S/N ~ 50 per resolution element.

2.2.3. Palomar Hale 5.0 m/Double Spectrograph

We observed K2-26 using the Double Spectrograph (DBSP, Oke & Gunn [1982](#)) at the Palomar observatory Hale 5.0 m telescope on 2015 February 12 UT. On the blue side of the spectrograph the 600 l/mm grating blazed at 3780 Å was used at a setting of $29\rlap{.}°5$. On the red side the 600 l/mm grating blazed at 9500 Å was used at an angle of $32\rlap{.}°5$. The star was observed with a $1''$ slit that provided a spectral resolution of $R \sim 2400$ and wavelength coverage from ~ 4000–7000 Å on the blue side and $R \sim 3000$ and coverage from ~ 7000–10000 Å on the red side. The target was observed at an air mass of 1.0 and conditions were generally favorable with seeing of about $1\rlap{.}''5-1\rlap{.}''8$. Standard IRAF functions (*apall*, *standard*, *sensfunc*)[23] were used to calibrate the data including bias frame subtraction and flat-fielding using dome flats; wavelength calibration using Fe–Ar arcs in the blue and He–Ne–Ar arcs in the red; and initial flux calibration with respect to standard Hiltner 600 (Hamuy et al. [1994](#)). A separate IDL routine was used to stitch together the red and blue spectra. A 4000–10000 Å portion is shown in Figure [5](#). For comparison, we also show the spectrum of the M1 standard star GJ 229 (Kirkpatrick et al. [1991](#); Maldonado et al. [2015](#)) observed using the same DBSP settings.

2.2.4. Keck/HIRES

We observed both stars using the High Resolution Echelle Spectrometer (HIRES, Vogt et al. [1994](#)) on the 10.0 m Keck I telescope. We observed the stars following standard California Planet Search (CPS, Marcy et al. [2008](#)) procedures using the C2 decker and the $0\rlap{.}''87 \times 14\rlap{.}''0$ slit. The $0\rlap{.}''87$ slit provides wavelength coverage from ~ 3600–8000 Å at a resolution of $R \approx 60,000$. No Iodine cell was used for these observations and the wavelength scale was calibrated using the standard HIRES reference. K2-26 was observed on UT 2015 February 5 and UT 2015 November 15 under good conditions with $\sim 1\rlap{.}''0$ seeing for a total of 565 s on each night. K2-9 was observed on UT 2015 July 12 under clear skies with $1\rlap{.}''4$ seeing for a total of 1200 s. These data were reduced using the standard pipeline of the CPS (Marcy et al. [2008](#)). The resulting spectra of K2-26 and K2-9 had S/Ns ~ 30 and 25 per pixel at 5500 Å, respectively. Examples of the HIRES spectra for both stars are shown in Figure [8](#).

---

[21] http://irtfweb.ifa.hawaii.edu/~spex/IRTF_Spectral_Library/

[22] IRAF is distributed by the National Optical Astronomy Observatories which are operated by the Association of Universities for Research in Astronomy, Inc., under cooperative agreement with the National Science Foundation.

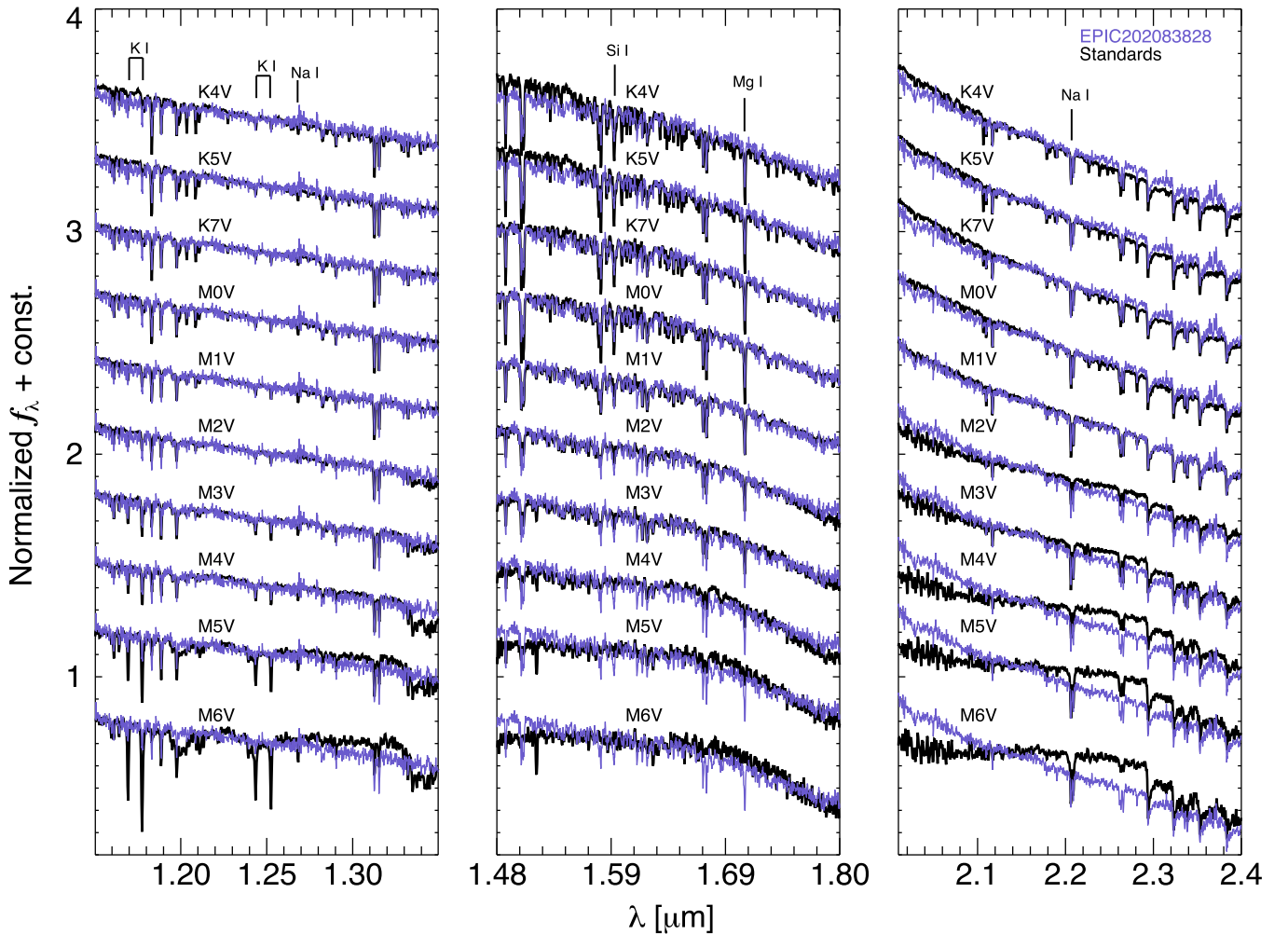[23] http://www.twilightlandscapes.com/IRAFtutorial/IRAFintro_06.html

Figure 3. *JHK*-band IRTF/SpeX spectra of K2-26 (EPIC 202083828) compared with late-type standards from the IRTF spectral library. All spectra are normalized to the continuum in each of the plotted regions. The star is a best visual match to spectral type M1 across the three near-IR bands. This is consistent with the results from our analyses using spectroscopic indices.

2.3. Adaptive Optics and Archival Imaging

2.3.1. LBT—LBTI/LMIRcam

K2-26 was observed on 2015 January 07 UT using the *L/M*-band Infrared Camera (LMIRcam, Skrutskie et al. 2010; Leisenring et al. 2012) of the Large Binocular Telescope (LBT) Interferometer (LBTI, Hinz et al. 2008). LBTI/LMIRcam is mounted at the bent Gregorian focus of the dual 8.4 m LBT and works in conjunction with the deformable secondary LBT Adaptive Optics system (LBTIAO, Esposito et al. 2010, 2011; Riccardi et al. 2010; Bailey et al. 2014) to deliver high-resolution, near-IR imaging. For our observations we only used the right side of the LBT. K2-26 was observed using the K_s-band filter ($\lambda_c = 2.16\,\mu$m, $\Delta\lambda = 0.32\,\mu$m) following a two-point dither pattern for sky subtraction. We obtained 40×0.15 s exposures using the target as a natural AO guide star for a total integration time of 6 s. Our data reduction included corrections for detector bias, sky background, and bad pixels followed by frame re-centering and averaging. The reduced image has a field of view (FOV) of 10″9 and a plate scale of 10.707 ± 0.012 mas pixel^{-1} (Maire et al. 2015). To ensure optimal background subtraction and contrast, the final image of K2-26 is trimmed to a 4″0 region of full dither overlap. This is shown in the inset of the left panel of Figure 6.

2.3.2. Palomar 60 Inch/Robo-AO

We acquired visible-light adaptive optics images of K2-26 using the Robo-AO system (Baranec et al. 2013, 2014) on the 60-inch Telescope at Palomar Observatory. On 2015 March 8 UT, we observed K2-26 with a long-pass filter cutting on at 600 nm (*LP*600) as a sequence of full-frame transfer detector readouts from an electron-multiplying CCD at the maximum rate of 8.6 Hz for a total of 120 s of integration time. The individual images are corrected for detector bias and flat-fielding effects before being combined using post facto shift-and-add processing using K2-26 as the tip-tilt star with 100% frame selection to synthesize a long-exposure image (Law et al. 2014). The resulting reduced image has a nominal FOV of 44″0 and plate scale of 0″0216 pixel^{-1} (Baranec et al. 2014). A 15″5 portion of the Robo-AO image centered on K2-26 is shown in the inset of the center panel of Figure 6. A faint, widely separated companion was detected in the Robo-AO image and is described in Section 3.3.1.
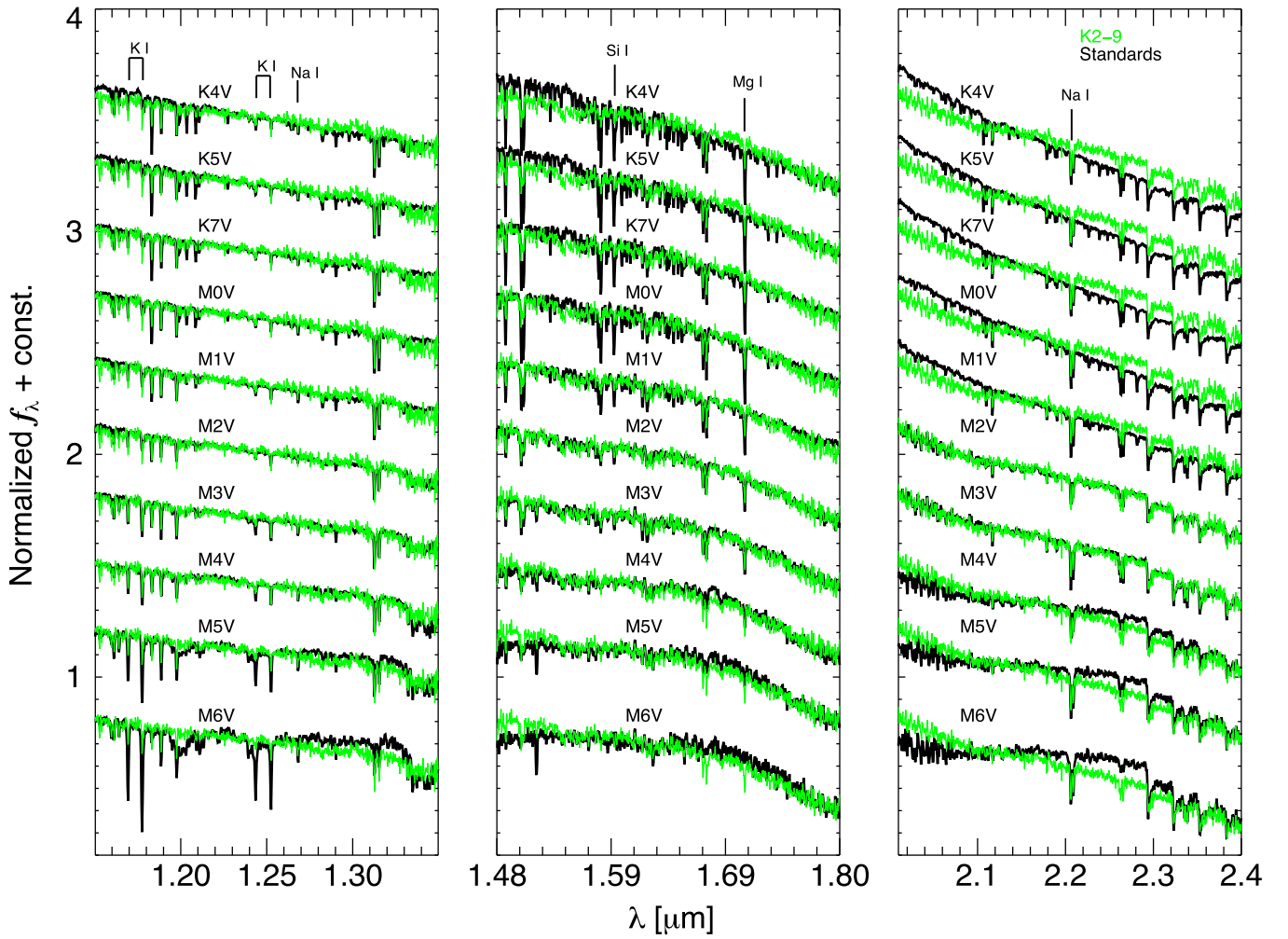
Figure 4. *JHK*-band IRTF/SpeX spectra of K2-9 compared with late-type standards from the IRTF spectral library. All spectra are normalized to the continuum in each of the plotted regions. The star is a best visual match to spectral type M2/M3 across the three near-IR bands. This is consistent with the spectral type derived from spectroscopic index-based methods.
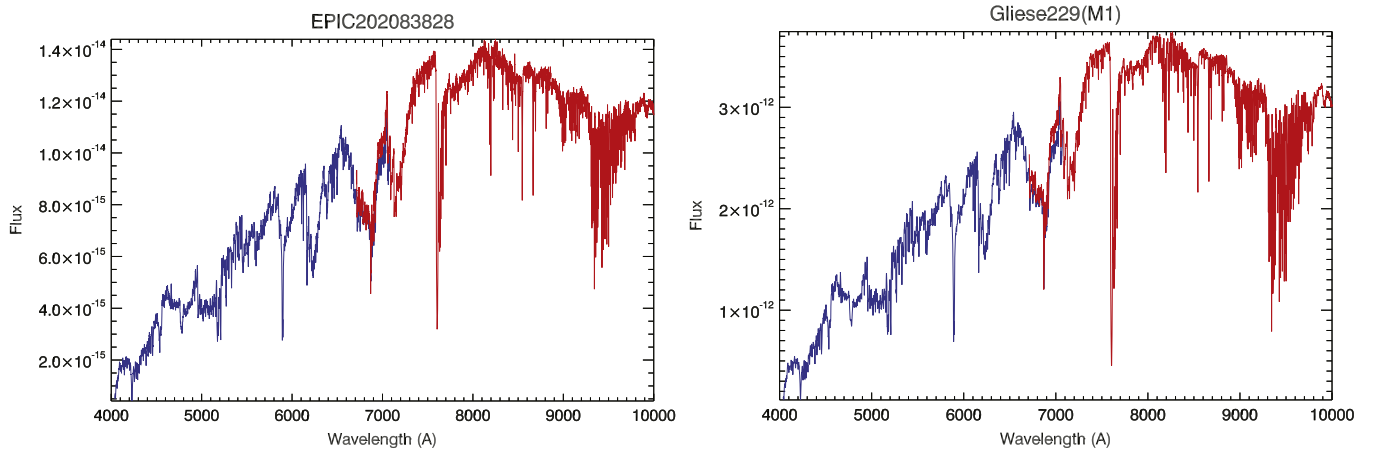

Figure 5. Left: spectra of K2-26 (EPIC 202083828) taken with the blue and red sides of the Double Spectrograph (DBSP) at the Palomar Hale 5.0 m. The flux units are arbitrary. Right: a comparison spectrum of the M1 standard star GJ 229. The overall continuum shape and strength of the deep broad molecular features (TiO, CaH, VO) of K2-26 are an excellent match to the M1 standard across the observed wavelength range.

2.3.3. Keck/NIRC2

We observed K2-9 using the Near Infrared Camera 2 (NIRC2) and laser guide star AO (LGS AO, van Dam et al. 2006; Wizinowich et al. 2006) on the 10.0 m Keck II telescope on 2015 April 07 UT. The target was observed in the K_p-band filter ($\lambda_c = 2.124\,\mu$m, $\Delta\lambda = 0.351\,\mu$m) using the narrow camera setting with a pixel scale of 9.942 mas pixel^{-1}. To avoid the noisier lower-left quadrant of the NIRC2 array,
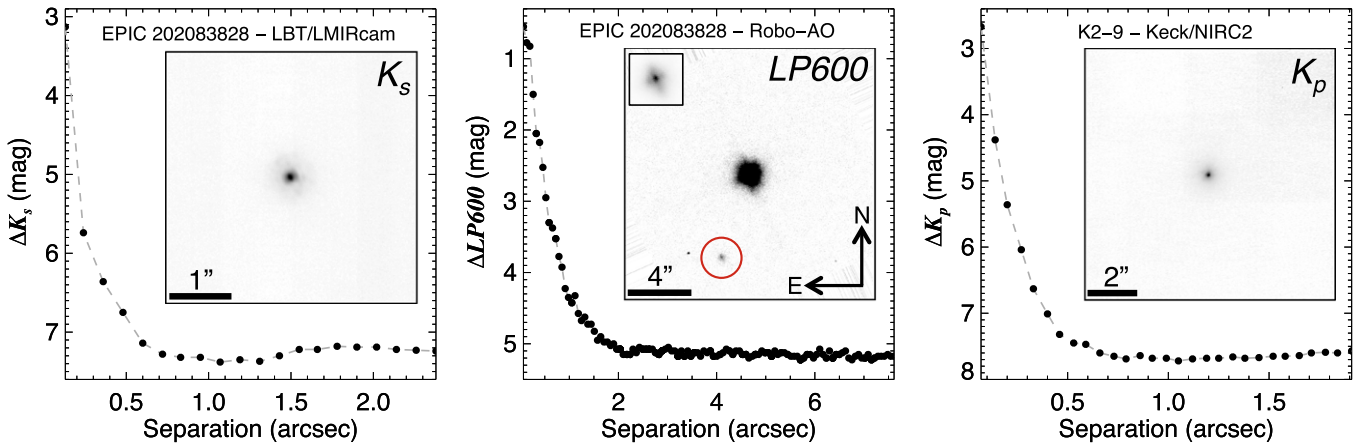
Figure 6. AO images and contrast curves for K2-26 (EPIC 202083828) and K2-9 Left: K2-26 LBT/LMIRcam K_s-band image (inset) and contrast curve. No additional stars are detected within $2\rlap{.}{''}0$. Center: K2-26 Robo-AO LP600-band image (inset) and contrast curve. An additional star is detected with $\Delta LP600 = 5$ mag at $5\rlap{.}{''}5$ separation (red circle). The small box in the upper left of the inset shows K2-26 without the hard stretch necessary to reveal the faint companion. Right: K2-9 Keck/NIRC2 K_p-band image and contrast curve. No additional stars are detected in the NIRC2 field of view.

we employed a three-point dither pattern with 11×10s integrations per dither yielding a total on-source integration time of 330 s. Individual frames were flat-fielded and sky-subtracted and then shifted and coadded to produce the final $10\rlap{.}{''}2$ image. Our NIRC2 image of K2-9 is shown in the inset of the right panel of Figure 6.

2.3.4. DSS and SDSS Archival Imaging

K2-26 and K2-9 were both observed in two different photometric bands (blue and red; B and R) during The National Geographic Society—Palomar Observatory Sky Survey (POSS I, Minkowski & Abell 1963) and the Second Palomar Observatory Sky Survey (POSS II, Reid et al. 1991) using the 1.2 m Samuel Oschin Telescope. The original POSS photographic plates were scanned and digitized by the Space Telescope Science Institute and are now available for flexible download as the Digitized Sky Survey (DSS)[24] The digitized POSS I and II plates have plate scales of $1\rlap{.}{''}01$ pixel^{-1}. K2-26 was observed in the B- and R-bands during POSS I on 1954 November 22 UT and in the B-band during POSS II on 1996 January 13 UT. K2-9 was observed in both POSS I bands on 1952 January 31 UT and in the POSS II B-band on 1995 January 01 UT. Both stars were also observed in five photometric bands (u, g, r, i, z) during the Sloan Digital Sky Survey (SDSS, York et al. 2000) using the 2.5 m Sloan Foundation Telescope (Gunn et al. 2006). SDSS images have a plate scale of $0\rlap{.}{''}396$ pixel^{-1}. K2-26 and K2-9 were observed during the SDSS on 2006 November 11 UT and 2006 January 06 UT, respectively. The total time baselines between the POSS I and SDSS epochs for each star are 52 and 54 years, respectively. We obtained the publicly available imaging data in the form of $1\rlap{.}{'}0$ POSS I B, POSS II B, and SDSS DR7 (Abazajian et al. 2009) g images of the stars centered on their 2015 epoch positions using the NASA/IPAC Infrared Science Archive (IRSA) Finder Chart web interface.[25] These data are presented in Figure 7.

3. ANALYSES AND RESULTS

3.1. Spectroscopic Analyses

3.1.1. Medium-resolution Spectroscopy

We use molecular band indices in the optical and near-IR to estimate spectral types (SpTy) for K2-26 and K2-9. The EFOSC2 spectrum of K2-26 provides access to TiO and CaH molecular bands that are temperature-sensitive and calibrated to provide SpTy's for stars ~K7-M6. We specifically use the TiO5, CaH2, and CaH3 indices (Reid et al. 1995; Gizis 1997) to estimate the stars' SpTy using the calibrated relations in Lépine et al. (2013). We find K2-26 has an optical SpTy of M1.0. The Lépine et al. (2013) relations have an accuracy of 0.5 subtypes. We also compare the EFOSC spectrum to optical M dwarf standard spectra from Kirkpatrick et al. (1991) and find a best visual match to types M1.0/M1.5. We perform a similar comparison of our DBSP spectra to M dwarf standards and find a consistent best match to the M1 standard GJ 229 (Figure 5). In the near-IR K-band, the H_2O-$K2$ index measures temperature-sensitive water opacity and is calibrated for SpTy's M0-M9 (Rojas-Ayala et al. 2012). We use our SpeX spectra to measure this index in EPIC 202083828 and K2-9 and find SpTy's of M1.0 and M2.5, respectively. The H_2O-K2/SpTy relation has a systematic scatter of 0.6 subtypes. Following these results we adopt a SpTy of M1.0 ± 0.5 for K2-26 and M2.5 ± 0.5 for K2-9. Our index-based measurements are consistent with the visual best matches to M dwarf standards (e.g., Figures 3 and 4) and are also consistent with SpTy estimates using the stars' optical and near-IR colors (Pecaut & Mamajek 2013).[26]

Following Crossfield et al. (2015), we use our SpeX spectra to estimate the fundamental parameters of metallicity ([Fe/H]), effective temperature ($T_{\rm eff}$), radius (R_*), and mass (M_*) for K2-26 and K2-9 using the methods presented in Mann et al. (2013a, 2013b). In these works, metallicity is estimated using the spectroscopic index and equivalent width (EW)-based methods (Rojas-Ayala et al. 2012; Terrien et al. 2012; Mann et al. 2013b) that were calibrated using a sample of M dwarfs

――――――――
[24] http://stdatu.stsci.edu/cgi-bin/dss_form
[25] http://irsa.ipac.caltech.edu/applications/finderchart/

[26] Throughout this work we use the expanded table available on Eric Mamajek's webpage: http://www.pas.rochester.edu/~emamajek/EEM_dwarf _UBVIJHK_colors_Teff.txt
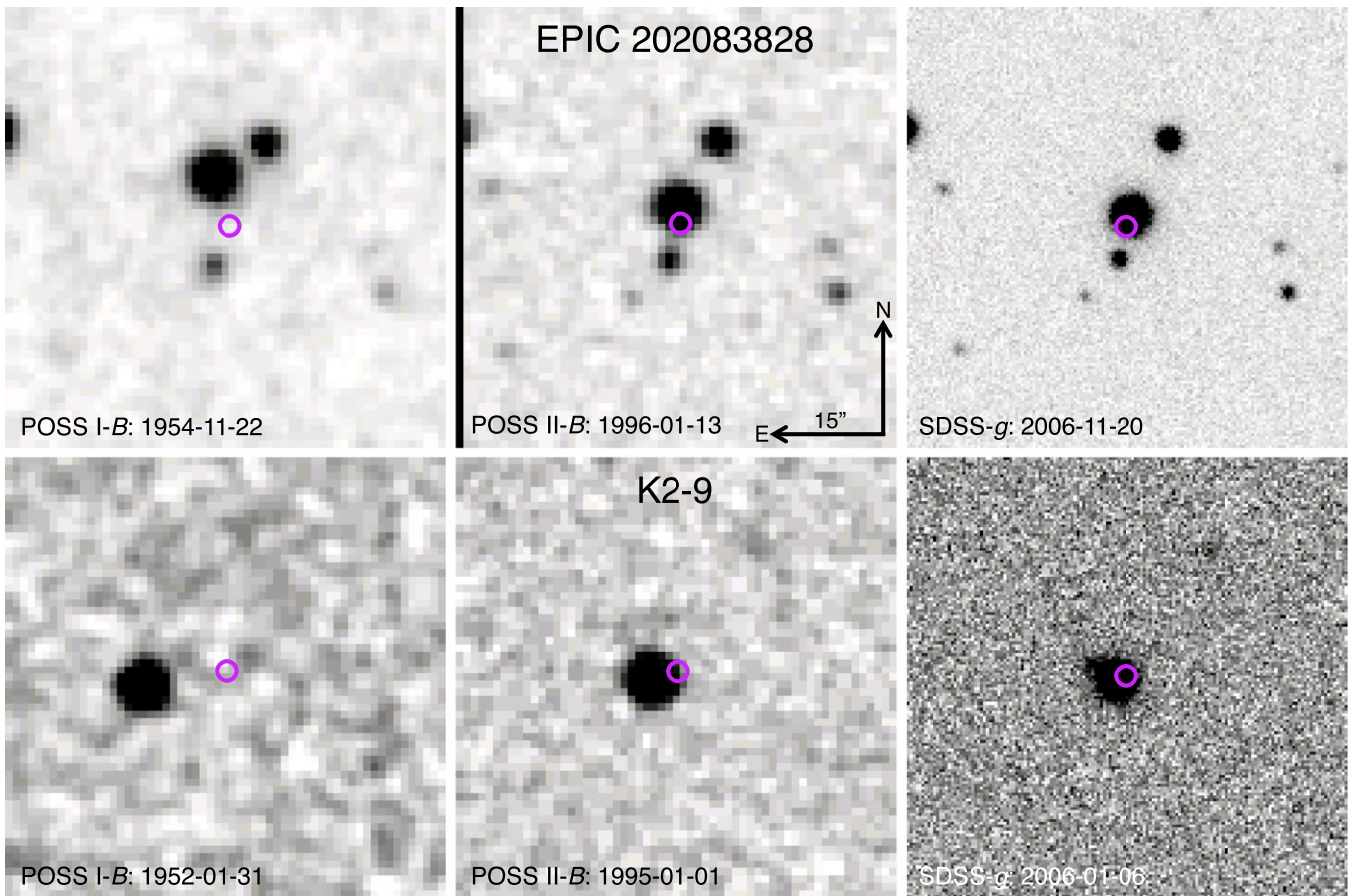
Figure 7. $1\rlap{.}'0 \times 1\rlap{.}'0$ archival survey images of K2-26 (EPIC 202083828) and K2-9. Top: K2-26 DSS and SDSS images displaying $>6''$ of transverse motion over 52 years. The faint star in the south–southeast of each image is the same as revealed in our Robo-AO images. The star is not co-moving with K2-26. Bottom: DSS and SDSS images of K2-9 showing $>9''$ of transverse motion over 54 years. A very faint source is detected $\sim3\rlap{.}''5$ to the northeast of K2-9 in the SDSS image and appears as an extension of the K2-9 intensity distribution. This source is not detected with confidence in the shallower POSS images. Further details are provided in Section 3.3.2. The POSS I images reveal no stars at the current positions of K2-26 or K2-9 (magenta circles) down to the photometric limits of that survey.

having wide, co-moving FGK companions with well-determined [Fe/H]. We use IDL software made publicly available by A. Mann[27] to calculate the metallicities of K2-26 and K2-9 in the H- and K-bands. We average the H and K metallicities and add the measurement and systematic uncertainties in quadrature to arrive at the final values. We find K2-26 has [Fe/H] $= -0.13 \pm 0.15$ and K2-9 has [Fe/H] $= -0.25 \pm 0.20$. Thus neither star is metal-rich.

Effective temperature, radius, and mass are calculated using temperature-sensitive spectroscopic indices in the JHK-bands (Mann et al. 2013a) and empirical relations calibrated using nearby bright M dwarfs with interferometrically measured radii (Boyajian et al. 2012). We calculate $T_{\rm eff}$ in the JHK-bands and average the results. Conservative $T_{\rm eff}$ uncertainties are estimated by adding in quadrature the rms scatter in the JHK-band values and the systematic error in the empirical fits for each band (Mann et al. 2013a). The stellar radii, masses, luminosities, and densities are computed using publicly available software from A. Mann.[28] The resulting fundamental parameters are listed in Table 1. The larger relative uncertainties in R_* and M_* for K2-9 are a result of the poorer empirical fits in the Mann et al. (2013a) relations due to having

relatively few calibrators at low temperatures. Vanderburg et al. (2016) estimated $T_{\rm eff}$ and R_* for K2-26 using its $V - K$ color and found results consistent with ours. They also estimated $T_{\rm eff}$ and R_* for K2-9, this time using its $H - K$ color, and found values consistent with ours at $\sim2\sigma$. Additionally, Montet et al. (2015) estimated the fundamental parameters of K2-9 using broadband photometry and model fits. Our spectroscopic parameters are consistent with theirs in all cases within 1σ uncertainties, but our nominal values of mass, radius, and metallicity are all systematically larger. Photometric distances to the stars are estimated by calculating the distance moduli for their spectral types from the color-temperature conversion table of Pecaut & Mamajek (2013). We estimate K2-26 lies at 93 ± 7 pc and K2-9 at 110 ± 12 pc, just at the outer boundary of the extended solar neighborhood.

3.1.2. High-resolution Spectroscopy

We searched for tight spectroscopic binary companions or background stars at very close angular separations in our HIRES spectra using the methodology of Kolbl et al. (2015). The Kolbl et al. (2015) algorithm uses a library of more than 600 HIRES spectra of stars with a range of $T_{\rm eff}$'s, $\log(g)$'s, and metallicities to model the spectrum of the target star as the sum of two library templates and to search for secondary lines. For

---

[27] https://github.com/awmann/metal
[28] https://github.com/awmann/Teff_rad_mass_lum

high S/N targets, this method can detect companions within ∼0″8 of the primary, with as little as ∼1% of primary's flux in the V-band, and $\Delta RV > 10 \, \mathrm{km \, s^{-1}}$. The algorithm also measures the barycentric corrected primary RV via comparison to a standard solar spectrum.

Neither of our K2-26 spectra nor the spectrum of K2-9 exhibit evidence for a close-in, spectroscopic companion. Our analyses exclude tight companions as faint as 3% of the primary flux in the approximate V-band with $\Delta RV > 10 \, \mathrm{km \, s^{-1}}$. The lower flux limit corresponds to companions with $\Delta V \approx 3.8$. Assuming circular orbits and using the photometric relations in Pecaut & Mamajek (2013), our ΔV and ΔRV limits allow us to rule out companions ∼M4.5 and earlier at $\lesssim 0.7$ AU separations for K2-26 and companions ∼M5.0 and earlier at $\lesssim 0.7$ AU separations for K2-9. We measure $RV = 95.34 \pm 0.15 \, \mathrm{km \, s^{-1}}$ and $RV = 95.33 \pm 0.15 \, \mathrm{km \, s^{-1}}$ for K2-26 in 2015 February and November, respectively. We also measure $RV = -31.02 \pm 0.15 \, \mathrm{km \, s^{-1}}$ for K2-9. Our two RV measurements for K2-26 are separated by 281 days and are consistent within the $150 \, \mathrm{m \, s^{-1}}$ measurement uncertainty. These RV measurements are also consistent with the multi-epoch measurements spanning 28 days in Vanderburg et al. (2016). The consistency of these long-term RV measurements allows us to rule out RV accelerations due to companions below the sensitivity of our initial secondary line search. If we adopt our $150 \, \mathrm{m \, s^{-1}}$ HIRES measurement uncertainty as the maximum possible acceleration and assume circular orbits, our multi-epoch measurements rule out stellar mass companions at separations that overlap the limits from our LBT AO imaging (see Section 3.3.1) and a range of gas giant companions that includes $\gtrsim 2 M_{\mathrm{Jup}}$ at $\lesssim 0.25$ AU and $\gtrsim 5 M_{\mathrm{Jup}}$ at $\lesssim 1.5$ AU.

3.2. Activities, Kinematics, Ages, and Surface Gravities

The ∼6000–9000 Å (0.6–0.9 μm) region of M dwarf spectra provides access to several features sensitive to surface gravity and magnetic activity. Prior to the transition to fully convective interiors ($\lesssim$M4), M dwarfs lose angular momentum to a steady stellar wind and their rotation rates decrease over time. This decrease in rotation rate leads to a loss in dynamo-driven magnetic activity and a subsequent loss of high energy emission over time. Here we focus on emission from the 6563 Å Hα line as an activity indicator (West et al. 2008, 2011) to place constraints on the ages of K2-26 and K2-9. Our HIRES spectra of both K2-26 and K2-9 provide access to the Hα line at high resolution where it is seen in absorption in both stars (Figure 8). We used the IDL software line_eqwidth[29] to estimate EWs of 0.46 ± 0.02 Å and 0.34 ± 0.01 Å for K2-26 and K2-9, respectively. The Hα EWs suggest that both stars are relatively inactive, which is consistent with field age early M dwarfs (West et al. 2008). Our EFOSC2 and DBSP spectra of K2-26 cover the Hα line where it is also seen in absorption.

As an additional check of the stars' activity levels, we searched for excess ultraviolet (UV) emission using data from the NASA *GALEX* satellite (Martin et al. 2005). Like Hα, UV is tracer of magnetic activity in late-type stars and can be used to place limits on their ages (Shkolnik et al. 2011; Stelzer et al. 2013; Jones & West 2016). We searched the *GALEX* data using a 10″ radius centered on our targets in the GalexView

---
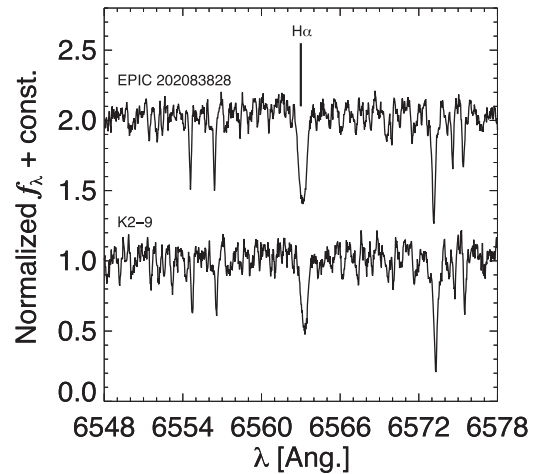[29] http://fuse.pha.jhu.edu/analysis/fuse_idl_tools.html
[30] galex.stsci.edu/GalexView/

Figure 8. RV corrected HIRES spectra of K2-26 (EPIC 202083828) and K2-9 centered on the Hα line at 6563 Å. The line is seen in absorption in both stars indicating they are relatively inactive and likely $\gtrsim$1 Gyr old.

Web Tool.[30] No *GALEX* observations are available for K2-26. K2-9 was observed by *GALEX* during the Medium Imaging Survey (MIS, Martin et al. 2005) in the far- and near-UV (FUV, NUV) bands. The star was detected at ∼4σ and ∼5σ in the FUV and NUV bands, respectively. The MIS observations spanned 2006 October to 2009 April. Following Shkolnik et al. (2011) and Schlieder et al. (2012b), we calculate the ratio of the FUV and NUV flux densities to the 2MASS J and K_s-band flux densities and compare them with samples of M dwarfs with known ages. The flux density ratios indicate that K2-9 has FUV and NUV emissions consistent with stars of similar SpTy having relatively large excess emission and young ages. When compared to the M dwarf samples with known ages in Shkolnik & Barman (2014), the fractional UV excesses suggest that K2-9 is at most as old as the Hyades (600–800 Myr, Perryman et al. 1998; Brandt & Huang 2015a, 2015b). It is possible that one of the epochs of the *GALEX* measurements caught the star during a flare or other transient period of heightened activity. UV flare events were observed in ∼3% of field M dwarfs in the variability survey of Welsh et al. (2007), and France et al. (2013) observed flares with timescales of 100–1000 s in *Hubble Space Telescope* UV spectra of field-age M dwarf planet hosts. These events are likely contributors to the measured ranges of UV activity in M dwarf samples of known age (up to 2 orders of magnitude, Shkolnik & Barman 2014). Therefore, the evidence for at least transient-strong UV emission from K2-9 is intriguing and may affect the properties of its planet, but when considered along with the large scatter of M dwarf UV excesses and the star's lack of Hα emission, it does not indicate that the star is strikingly young. We note that the ∼80 day *K2* light curve of K2-9 does not exhibit convincing evidence for magnetic spot-modulated variability or strong flares.

We investigate the kinematics of K2-26 and K2-9 by calculating their *UVW* Galactic velocities following the methods outlined in Johnson & Soderblom (1987) updated to epoch J2000.0. We adopt a solar-centric coordinate system where U is positive toward the Galactic center, V is positive in the direction of solar motion around the Galaxy, and W is positive toward the north Galactic pole. Using the measured proper motions and RV's and estimated distances, we calculate $UVW_{\mathrm{K2-26}} = (-91.7, \, -52.0, \, -28.7) \pm (2.1, \, 3.6, \, 2.2) \, \mathrm{km \, s^{-1}}$

and $UVW_{K2-9} = (-86.3, -8.1, -41.6) \pm (9.6, 3.1, 2.0)$ km s^{-1}. These estimates yield total Galactic velocities of $S_{K2-26} = 109.3$ km s^{-1} and $S_{5501} = 96.1$ km s^{-1}. Both stars have S consistent with the statistically older and kinematically hotter thick-disk population following the kinematic subdivisions of Bensby & Feltzing (2010). Their kinematics are thus consistent with other old M dwarfs. Alone, neither the lack of Hα emission nor the large Galactic velocities of K2-26 and K2-9 place strong constraints on their ages. However, when combined these observations suggest that both stars are $\gtrsim 1$ Gyr old. The observed UV excess of K2-9 warrants further consideration and is detailed in the context of its planet in Section 4.

Spectroscopic akali lines are sensitive to electron pressure in stellar atmospheres in the sense that increases in pressure lead to lines with broader wings (pressure broadening); thus in low pressure (low gravity) atmospheres, alkali lines are comparatively weak (Schlieder et al. 2012a). To verify that K2-26 and K2-9 are dwarf stars with high surface gravities, we investigate the gravity-sensitive Na I doublet near 8190 Å. After reducing our spectra to a resolution of $R \sim 900$, we measured the Na I index as defined by Lyo et al. (2004) and compared with samples with known surface gravities. For K2-26 we use the EFOSC2 spectrum to measure an Na I index of 1.064 ± 0.023. We prefer the EFOSC2 spectrum over the SpeX spectrum for this measurement since the S/N is $\sim 6\times$ greater at 8200 Å. For K2-9, we have only the SpeX spectrum with an S/N ~ 20 at 8200 Å and measure an Na I index of 1.144 ± 0.129. The Na I uncertainties are estimated using MC methods. When compared with the dwarf, young, and giant samples in Lawson et al. (2009), both K2-26 and K2-9 are consistent with the field M dwarf sequence within uncertainties. This is reinforced by our initial target selection using reduced proper motion diagrams (which removes giants) and the visual matches of their SpeX spectra to M dwarf standards (Figures 3 and 4).

3.3. Imaging Analyses

3.3.1. Adaptive Optics Imaging

In our LBT/LMIRcam imaging, K2-26 was measured with a resolution of 0″116 (FWHM) and appears single at that limit. No other stars were detected in the 4″0 region of full dither overlap. We estimate the sensitivity to faint companions and background stars by injecting fake point sources with an S/N = 5 into the final image at separations $N\times$ FWHM where N is an integer. The 5σ sensitivities as a function of separation are shown in the left panel of Figure 6. Our LMIRcam imaging is sensitive to stars with K_s-band contrast $\Delta K_s = 3.1$ mag at 0″1 separation and $\Delta K_s = 7.2$ mag at $\geqslant 0″5$ separation. At the distance of K2-26 and ages $\gtrsim 1$ Gyr, these magnitude limits correspond to $\sim$M5 and earlier companions at $\gtrsim 9$ AU and substellar companions at $\gtrsim 47$ AU (Pecaut & Mamajek 2013; Baraffe et al. 2015).

Our Robo-AO images of K2-26 measure the star at the diffraction limit of 0″15 (Baranec et al. 2014). We detect an additional star with ΔLP600 = 5.02 ± 0.07 mag at 5″53 to the southeast. In the inset of the center panel in Figure 6 we show K2-26 with a hard stretch and highlight this star with a red circle. This source falls within the 2 pixel (8″) software aperture used to extract the K2 photometry. However, with ΔLP600 ~ 5 (LP600 $\approx$ Kep) it contributes only $\sim$1% of the flux in the aperture and would have to harbor a deeply eclipsing

stellar companion to account for the measured $\sim$0.3% transit depth. We discuss this possibility further in Section 3.4. We place limits on the presence of other stars in the Robo-AO image by masking out the faint companion, replacing its flux with the median background at its separation, and performing the multiple levels of automated companion search described in Law et al. (2014). These searches identify no additional companion candidates and provide 5σ sensitivity limits as a function of separation (center panel of Figure 6). Our Robo-AO imaging rules out stars with ΔLP600 $\leqslant 5$ mag beyond the 2″0 radius of our much more sensitive LMIRcam image. At the distance of K2-26, this sensitivity corresponds to $\sim$M5 companions at $\gtrsim 194$ AU.

The Keck/NIRC2 image of K2-9 reveals the star with a resolution of 0″066 (FWHM) and it appears single at that limit. No other stars were detected in the full field of view of the image. We estimate the sensitivity to faint companions and background stars following the same procedure described for the LMIRcam image of K2-26. The 5σ sensitivities as a function of separation are shown in the right panel of Figure 6. Our NIRC2 imaging is sensitive to stars with K_p-band contrast $\Delta K_p = 3.5$ mag at 0″1 separation and $\Delta K_p = 7.5$ mag at $\geqslant 0″5$ separation. At the distance of K2-9 and ages $\gtrsim 1$ Gyr, these magnitude limits correspond to $\sim$M7 companions at $\gtrsim 11$ AU and substellar companions at $\gtrsim 55$ AU (Pecaut & Mamajek 2013; Baraffe et al. 2015). Since both K2-26 and K2-9 are within approximately 100 pc of the Sun, reddening by interstellar dust is assumed to have a negligible effect and is not taken into account in our estimates of companion detection limits.

3.3.2. Archival DSS and SDSS Imaging

Both K2-26 and K2-9 have total proper motions of $>0″1$ yr^{-1}. Over the time baseline between their POSS I and SDSS observations, K2-26 has moved $\sim 6″3$ and K2-9 has moved $\sim 9″4$. We display this large transverse motion in Figure 7 where the subpanels are centered on the stars' epoch 2015 coordinates (magenta circles). The left column of Figure 7 reveals that there are no background sources at the current positions of the stars down to the POSS I B limit of 21.1 mag (Abell 1955). We also find no background sources down to the POSS I R limit of 20.0 mag (Abell 1966). If there are background sources at the current position of K2-26, they must be $B \sim 5$ mag and $R \sim 7$ mag fainter. For K2-9, undetected background sources must be $B \sim 4.5$ mag and $R \sim 6$ mag fainter. The archival images also reveal a star to the southeast of K2-26. This source, SDSS J061649.67+243539.9, lies 6″3 away in the SDSS epoch (2006.9) and has a relatively small proper motion of 32.9 mas yr^{-1} to the north-northwest (Abazajian et al. 2009; Roeser et al. 2010) and is thus not co-moving with K2-26. The position angle and separation in the SDSS image are consistent with this star being the same as that revealed in our Robo-AO image. SDSS J061649.67+243539.9 is 4.2 mag fainter than K2-26 in the SDSS g-band and its SDSS7 and 2MASS photometry are consistent with a K5 $\pm$ 2 spectral type (Kraus & Hillenbrand 2007; Pecaut & Mamajek 2013) assuming no reddening. With $J = 16.37$, a $\sim$K5 star would be $\sim$1.8 kpc distant and lie far behind K2-26. The SDSS g image of K2-9 reveals a very faint source at only 3″5 to the northeast where the object appears as an extension to the K2-9 intensity distribution. This source, SDSS J114503.63+000021.4, has $r = 22.8$ and is undetected in

other archival surveys (DSS, 2MASS, etc.). Thus, no proper motion measurements are available. The source is also undetected in our NIRC2 images of K2-9 which have a 5σ sensitivity at wide separations of $K \sim 19$ mag. Regardless of the nature of this object, we estimate that it contributes negligible flux ($\sim 0.1\%$) to the $K2$ software aperture.

3.4. Light Curve Validation and FPPs

After TERRA identifies candidate transits, it runs a suite of diagnostics to vet out possible astrophysical false positives such as eclipsing binaries, spot modulation, or periodic stellar variability. K2-26 and K2-9 both passed these tests and were subject to further extensive testing to explore centroid motions in and out of transit, difference imaging analyses, and pixel correlation images (e.g., Bryson et al. 2013). Both stars passed these further checks and we found it unlikely that the observed transits associated with K2-26 occurred around the faint star observed to the southeast in the Robo-AO and archival images. This is corroborated by independent *Spitzer* detections of the transit using a software aperture that excludes the nearby faint star (see Beichman et al. 2016).

Other possible scenarios that could give rise to the observed transits are an unblended EB, unresolved bound companions hosting their own transiting stellar or planetary companion, or background EBs. Our Keck/HIRES and AO imaging analyses have ruled out a wide range of bound companions. Given these constraints, the radius of a potential planet around any undetected bound companion would have to be improbably large to produce the measured transit depths when considering the dilutions from K2-26 and K2-9 (Dressing & Charbonneau 2013, 2015). The lack of detectable stars at the current positions of K2-26 and K2-9 in POSS I images also places strong constraints on unresolved background eclipsing binaries not ruled out by our spectroscopy and imaging.

As a final check, we estimate the likelihood that our observed transits are false positives rather than bona fide planetary systems using the open source FPP calculator vespa (Morton 2012, 2015).[31] To calculate FPPs, this software package compares the typical light curve shapes of a distribution of astrophysical false positive scenarios with the observed transit light curve and combines that information with prior assumptions about stellar populations, multiplicity frequencies, and planet occurrence rates. The false positive scenarios tested are an unblended EB, a blended background EB, a hierarchical companion EB, and the "double period" EB scenario, which is newly implemented in vespa. A key input to vespa in the standard EB scenarios is the secondary depth constraint, $\delta_{\mathrm{sec,max}}$, which is the deepest secondary event allowed at all phases. This is determined by masking the transit signal of the candidate planet and searching the light curve for the most significant signal at the same period (see Morton 2012; Montet et al. 2015). The newly implemented "double period" scenario in vespa is the hypothesis that the transit signal is caused by an EB (either unblended, background, or hierarchical) at double the measured period where the primary and secondary eclipses are the same depth. This case cannot be subject to the same secondary depth constraint as the others; rather, it is subject to an odd–even constraint that requires the primary and secondary eclipses have depths within $\sim 3\sigma$ of the photometric uncertainty in the phase-folded light curve.

Table 2
False Positive Probability Calculation Results

Param	K2-26b	K2-9b
$\delta_{\mathrm{sec,max}}$ [ppt][a]	0.24	0.47
$\mathrm{Pr_{EB}}$	$<10^{-4}$	$<10^{-4}$
$\mathrm{Pr_{DPEB}}$	$<10^{-4}$	$<10^{-4}$
$\mathrm{Pr_{BEB}}$	2.4×10^{-3}	$<10^{-4}$
$\mathrm{Pr_{DPBEB}}$	$<10^{-4}$	$<10^{-4}$
$\mathrm{Pr_{HEB}}$	$<10^{-4}$	$<10^{-4}$
$\mathrm{Pr_{DPHEB}}$	$<10^{-4}$	$<10^{-4}$
f_p [b]	0.21	0.20
FPP	3.2×10^{-3}	2.4×10^{-5}
Planet?	Yes	Yes

Notes.
[a] Maximum secondary depth.
[b] Integrated planet occurence rate.

As additional inputs to vespa, we used our phase-folded light curves, the stellar photometry from APASS, 2MASS, and *WISE*, the stars' physical parameters listed in Table 1, our near-IR AO contrast curves, the constraints on background stars from the POSS I *R*-band archival images, and our HIRES RV constraints implemented as a velocity contrast curve in vespa (e.g., Marcy et al. 2014).We ran vespa within 5″.0 and 12″.0 of K2-26 and K2-9, respectively. The K2-26 aperture was chosen to exclude the faint companion from our Robo-AO image which we have already ruled out as the transit host. In the absence of close companions, the K2-9 aperture was chosen to be consistent with the *K*2 photometric aperture. Table 2 lists the FPPs from each of the tested false positive scenarios.We find total FPPs of 3.2×10^{-3} and 2.4×10^{-5} for K2-26 and K2-9 respectively. The estimated FPPs are sufficiently low that we consider both systems to be validated exoplanets. Our vespa input files are available upon request.

3.5. Planet Parameters

We analyze the time-series photometry for these systems using an approach similar to the one described by Crossfield et al. (2015) that relies on the emcee Markov Chain Monte-Carlo (MCMC) package (Foreman-Mackey et al. 2013). We estimated these planets' parameters using two different light curve analysis packages: JKTEBOP (Southworth et al. 2004; Southworth 2011) and BATMAN (Kreidberg 2015). We also used both linear and quadratic limb-darkening (LD) relations. For the linear LD relation, we impose Gaussian priors on the LD parameter, determined by examining all linear LD terms tabulated by (Claret et al. 2012) that satisfy $3300 \leqslant T_{\mathrm{eff}} \leqslant 3700$ K and $\log_{10} g \geqslant 4.5$. For the prior, we take the mean and twice the standard deviation of these values to account for possible systematic uncertainties in the models (Espinoza & Jordán 2015). For the quadratic LD relation, we estimated parameters using the LDTk package (Parviainen 2015; Parviainen & Aigrain 2015).[32] LDTk calculates custom LD profiles and coefficients using a library of PHOENIX spectra. The uncertainties on the LD parameters are propagated from the uncertainties on the stellar parameters. For each light curve analysis package and both linear and quadratic LD, we

---

Table 3
Summary of Planet Properties

Param	Units	K2-26b	K2-9b
T_0	MBJD$^a_{TDB}$	$1942.1659^{+0.0028}_{-0.0021}$	$1989.6712^{+0.0025}_{-0.0033}$
P	day	$14.5665^{+0.0016}_{-0.0020}$	$18.4498^{+0.0015}_{-0.0015}$
i	degree	$88.4^{+1.2}_{-1.5}$	$87.983^{+1.593}_{-0.080}$
R_P/R_*	%	$4.71^{+0.37}_{-0.22}$	$6.669^{+0.060}_{-1.307}$
T_{14}	hr	$4.73^{+0.25}_{-0.12}$	$2.8397^{+0.0074}_{-0.5492}$
T_{23}	hr	$4.11^{+0.15}_{-0.44}$	$0.62^{+1.38}_{-0.27}$
R_*/a	⋯	$0.0483^{+0.0186}_{-0.0076}$	$0.0380^{+0.0011}_{-0.0208}$
b	⋯	$0.57^{+0.24}_{-0.39}$	$0.9261^{+0.0080}_{-0.4929}$
u	⋯	$0.566^{+0.048}_{-0.047}$	$0.579^{+0.105}_{-0.070}$
$\rho_{*,circ}$ [b]	g cm^{-3}	$0.79^{+0.53}_{-0.49}$	$1.010^{+9.870}_{-0.096}$
$\rho_{*,spec}$ [c]	g cm^{-3}	$3.92^{+1.43}_{-1.43}$	$9.88^{+4.25}_{-4.25}$
a	AU	$0.0962^{+0.0054}_{-0.0061}$	$0.091^{+0.013}_{-0.016}$
R_P	$R_\oplus$	$2.67^{+0.46}_{-0.42}$	$2.25^{+0.53}_{-0.96}$
S_{inc}	$S_\oplus$	~5.8	$1.36^{+1.59}_{-0.81}$
T_{eq}	K	~430	314^{+67}_{-64}
R_*	$R_\odot$	$0.520^{+0.080}_{-0.080}$	$0.31^{+0.11}_{-0.11}$
M_*	$M_\odot$	$0.560^{+0.100}_{-0.100}$	$0.30^{+0.14}_{-0.13}$

Notes.
[a] BJD—2454833.
[b] Stellar density from transit fits assuming circular orbits.
[c] Stellar density from spectroscopic stellar parameters.

assumed circular orbits and calculated the fit parameters. In every case we find consistent results. Thus, we adopt the fit parameters from JKTEBOP using linear limb-darkening for the remainder of our analyses (Table 3).

These fits provide planetary radii $R_{K2-26b} = 2.67^{+0.46}_{-0.42}\ R_\oplus$ and $R_{K2-9b} = 2.25^{+0.53}_{-0.96}\ R_\oplus$. Thus, both planets are small and have estimated radii near the transition between Earth-like rocky bodies and Neptune-like bodies with large gaseous envelopes (Marcy et al. 2014; Weiss & Marcy 2014; Rogers 2015). Our transit fits also provide an estimate of the stellar density, ρ_*. For K2-26, the stellar density from the fit is inconsistent with the density inferred from our spectroscopic constraints on the star's mass and radius (Table 3). This result is driven by the measured transit duration of 4.73 hr, ~1.8 hr longer than expected for a circular orbit with a low-impact parameter. The long transit duration can be explained either by the planet orbiting a low-density (giant) star with a large radius or by the planet having an eccentric orbit where the transit is observed away from periapse. This phenomenon is known as the photoeccentric effect (Dawson & Johnson 2012). Since our spectroscopic and other analyses conclusively demonstrate that K2-26 is a dwarf and not a giant, planetary eccentricity likely causes the long transit duration. In the case of K2-9 the larger uncertainties on the stellar parameters result in a larger uncertainty on the stellar density in the fit. Although the nominal value is inconsistent with the spectroscopic constraints, the full uncertainty range is consistent. We also find that the measured transit duration is consistent with expectations for an approximately circular orbit.

To further test these hypotheses, we examine the photoeccentric effect in post-processing of the posterior distributions to the MCMC transit analysis that assumed a circular orbit. The final unimodal distribution hints that K2-26 may have an eccentric orbit with a lower eccentricity limit of $e > 0.14$ with 95% confidence ($e > 0.01$ at 97% confidence). In addition, the

posterior on the argument of periapsis, ω, peaks near $270°$ which is consistent with our qualitative assessment that the transit occurs away from periapse. The same analysis of K2-9b provides a lower eccentricity limit of $e > 0.05$ at 95% confidence. This constraint supports our previous assessment that the orbit of K2-9b is approximately circular. We also performed a photoeccentric analysis on several dozen other planet candidates from our $K2$ sample and found only two other systems with evidence for eccentricity. In contrast to K2-26b, these candidates exhibited transit durations shorter than expected for a circular orbit with ω close to $90°$. As a final note, we mention that any photoeccentric analysis is subject to measurement bias such that any constraints on eccentricity are always positive and non-zero. Figures 1 and 2 show the resulting photometry and best-fit models and Table 3 summarizes the final planetary parameters and uncertainties.

4. DISCUSSION

4.1. K2-26b: A Temperate Sub-Neptune with Evidence for Eccentricity

K2-26b was the only candidate M dwarf planet found in our search of the $K2$ C0 data and is the first validated planet from that field. $K2$ C0 was anticipated to be the first full-length campaign for the spacecraft in its new observing mode but fine guiding control was only achieved for ~35 days, thereby limiting useful data to this period (Vanderburg 2014). The discovery of a small planet with a 14.57 day orbital period in only 35 days of data is both fortuitous and a testament to the quality of the $K2$ data. K2-26b belongs to a class of planets known as sub-Neptunes: planets smaller than Neptune with substantial H/He atmospheres (Marcy et al. 2014; Weiss & Marcy 2014; Rogers 2015). We estimate the mass of the planet and the likelihood that it is more dense than 100% silicate rock following the probabilistic approach described in Wolfgang et al. (2015) and Wolfgang & Lopez (2015). This approach uses a sample of known small planets with measured masses and radii, interior structure models, and hierarchical Bayesian modeling to fit a mass–radius relation to the data that includes measurement and systematic errors. Using software provided by A. Wolfgang[33], we find $M_{K2-26b} = 9.4 \pm 3.3\ M_\oplus$ and <3% probability that the planet is more dense than silicate rock. The deterministic fit described in Weiss & Marcy (2014) provides a nominally smaller but still consistent mass of ~6.7 $M_\oplus$.

To further investigate the hint of eccentricity in K2-26b, we searched the NASA Exoplanet Archive[34] (Akeson et al. 2013) for similar small planets to compare its eccentricity constraints to known systems. The database contains 63 transit or RV detected planets with $M_p < 1\ M_{Nep}$, $a < 0.4$ AU, and $e > 0$. In Figure 9 we show the eccentricities versus semimajor axes of these planets along with our K2-26b 95% confidence lower limit. Our K2-26b limit is larger than 65% of the sample. Only about 20% of the sample has eccentricities $\gtrsim 0.2$. These data are consistent with previous studies that found close-in exoplanets have average eccentricities smaller than planets on wider orbits, with most having $e < 0.2$ (Jackson et al. 2008b). This is likely due to tidal dissipation of both the eccentricity and semimajor axis over time which circularizes the orbits (Rasio et al. 1996). Thus, since K2-26b may have $e > 0.14$, the evolution of its
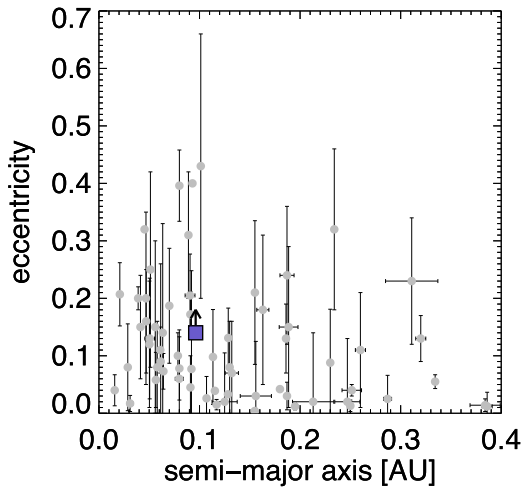
Figure 9. Eccentricity vs. semimajor axis for planets in the NASA Exoplanet Archive with separations less than 0.4 AU are less massive than Neptune and have non-zero eccentricities. Our K2-26b (EPIC 202083828b) 95% confidence lower eccentricity limit is shown as a slate-blue square.

orbit and its internal heat may be affected through tidal dissipation (Jackson et al. 2008a).

In the process of tidal dissipation, both the eccentricity and semimajor axis of a planet are reduced as orbital energy is converted into internal heat via tidal stresses. Thus, the rates of change of eccentricity, semimajor axis, and tidal heating are strongly coupled and only instantaneous values can be calculated outside of time-dependent numerical integrations. We use the relations provided in Jackson et al. (2008a, 2008b) to investigate these effects where we assume that the eccentricity is equal to our inferred 95% lower limit, $e = 0.14$. In this scenario we estimate the eccentricity and semimajor axis of K2-26b decrease by at least $\sim 3 \times 10^{-11}$ yr^{-1} and $\sim 8 \times 10^{-13}$ AU yr^{-1}, respectively. These estimates correspond to a minimum tidal heating of ~ 600 W m^{-2}. We also estimate the minimum orbit-averaged incident flux following Barnes et al. (2008) and find that $S_{\rm inc} \gtrsim 5.4\ S_{\oplus}$. Thus, the estimated tidal heating contributes at least an additional $\sim 8\%$ of the incident flux resulting in a total flux of $S_{\rm tot} \gtrsim 5.8\ S_{\oplus}$. This yields a zero albedo equilibrium temperature for K2-26b of $T_{\rm eq} \gtrsim 430$ K. The equilibrium temperature remains $\lesssim 500$ K for eccentricities $\lesssim 0.8$. Following the habitable zone (HZ) description of Kopparapu et al. (2013, 2014), the planet's current separation and our tidal dissipation timescale estimates indicate that K2-26b was likely never in the HZ of its host star. This holds true even for eccentricities much larger than $e = 0.14$.

A plausible explanation for the non-zero lower limit on the planet's eccentricity is the influence of an undetected perturber. Our multi-epoch HIRES RV measurements rule out a portion of mass/semimajor axis parameter space for $>1\ M_{\rm Jup}$ companions. However, additional bodies may still exist in the system and induce transit-timing variations (TTVs, Agol et al. 2005; Holman & Murray 2005) of K2-26b. We searched for TTVs in our 3 K2 transits of the planet by fitting for the central time in each transit individually, then fitting a straight line to the transit times as a function of transit number. Significant TTVs would be apparent when comparing the observed time of each transit with the best-fit linear ephemeris. We see no evidence of significant TTVs in the K2 data of K2-26b. However, if the

transits times are slowly varying, TTV signatures may be undetectable over the short-time baseline of the K2 C0 data (~ 35 days). Thus, future followup over a longer baseline is warranted and could still reveal evidence of a perturber via TTVs. Additional high-cadence photometry over a period longer than ~ 35 days and high-precision RV monitoring would also be useful to search for additional planets and for placing better constraints on the possible eccentricity of K2-26b.

4.2. K2-9b: A Transition Radius Planet Receiving Earth-like Insolation Orbiting a UV Active Star

The full range of estimated radii of K2-9b are consistent with the planet straddling the transition region between planets with Earth-like rocky/iron compositions and planets with Neptune-like volatile rich compositions (Rogers 2015). We use the same methods from Wolfgang et al. (2015) to estimate its mass and probability of rocky composition. From our estimated radius and an average symmetric radius uncertainty, we find that $M_{K2-9b} = 7.6 \pm 4.1\ M_{\oplus}$ and $\sim 21\%$ probability that it has an Earth-like rock/iron composition. The smaller but still consistent radius estimated by Montet et al. (2015) yields a mass of $4.7 \pm 2.9\ M_{\oplus}$ and $\sim 52\%$ probability of being more dense than silicate rock. Thus, K2-9b, like K2-3cd and K2-21b, is a transition radius planet having almost equal likelihood of either composition given current constraints on the densities and model inferred compositions of small planets. The deterministic mass–radius relation of Weiss & Marcy (2014) provides a mass of $\sim 4.9\ M_{\oplus}$ using the average radius estimated from our analyses and Montet et al. (2015).

The estimated flux from its host star incident on any atmosphere harbored by K2-9b is consistent with the flux received by the Earth from the Sun, $S_{\rm inc} = 1.36^{+1.59}_{-0.81}\ S_{\oplus}$. Its estimated semimajor axis places it just within the inner edge of the star's optimistic HZ (Kopparapu et al. 2013, 2014). The incident flux corresponds to an equilibrium temperature of $T_{\rm eq} = 315^{+67}_{-64}$ K. In the case that the planet is rocky and has favorable atmospheric, cloud, and surface properties, liquid water could exist on K2-9b. This potential is particularly interesting when the measured UV flux of the host star is considered.

Whether the large GALEX UV flux of K2-9 is constant or transient, this emission dominates the photochemistry of any atmosphere its planet harbors. UV photons photodissociate key molecules including H_2O, CH_4, and CO_2 (Kasting et al. 1993; Segura et al. 2010) and can lead to the formation of high-level hazes. Such hazes have been inferred from the transmission spectrum of GJ 1214b, a small planet orbiting an M dwarf (Charbonneau et al. 2009; Bean et al. 2011; Kreidberg et al. 2014). UV flux can also cause atmospheric loss via photoevaporation (Luger & Barnes 2015, and references therein). For the case of intransient UV emission we estimate the flux from the strongest stellar UV emission line, the resonance line of hydrogen at 1215.7 Å, Lyα. We calculate the Lyα flux ($F_{\rm Ly\alpha}$) from K2-9's GALEX UV fluxes using the relations in Shkolnik et al. (2014). These fits were calibrated using reconstructed intrinsic Lyα fluxes from a sample of K and M dwarfs with UV spectra from the Hubble Space Telescope (MUSCLES, France et al. 2013; Linsky et al. 2013). All fluxes in these calculations are scaled to the surface of the star using our photometric distance and the measured stellar radius. We estimate the $F_{\rm Ly\alpha}$ at the surface of K2-9 is $\sim 2.5 \times 10^6$ erg cm^{-2} s^{-1}. This corresponds to a $S_{\rm Ly\alpha}$ at the

planet of $\sim 8500\,\mathrm{erg\,cm^{-2}\,s^{-1}}$, nearly $5\times$ larger than the estimated $S_{\mathrm{Ly}\alpha}$ at the sub-Neptune GJ436b (France et al. 2013; Miguel et al. 2015). If K2-9b harbors an atmosphere, the upper portions could therefore receive a UV flux where models predict significant chemical changes (Miguel et al. 2015) and possible atmospheric loss (Luger & Barnes 2015). If the strong *GALEX* UV flux was the result of a flare, the presumed atmosphere of the planet may be less affected (Segura et al. 2010).

4.3. Prospects for Follow-up

Both K2-26b and K2-9b are small temperate planets that orbit close to low-mass stars. We assume circular orbits and adopt the nominal masses from the Wolfgang & Lopez (2015) probabalistic mass–radius relation to estimate stellar RV semi-amplitudes of $K_{\mathrm{K2\text{-}26b}} \sim 3.6\,\mathrm{m\,s^{-1}}$ and $K_{\mathrm{K2\text{-}9b}} \sim 4.1\,\mathrm{m\,s^{-1}}$. These predicted reflex velocities are within the reasonable limits of current ground-based, high-precision spectrometers (e.g., HIRES and HARPS), but the stars are too faint at visible wavelengths. These planets along with others being discovered by *K2* (i.e., Hirano et al. 2015) may be ideal targets for next-generation spectrometers operating in the IR where M dwarfs are brighter (e.g., CARMENES, SPIRou, IRD, HPF, Artigau et al. 2014; Kotani et al. 2014; Mahadevan et al. 2014; Quirrenbach et al. 2014). High-precision RVs will provide planet masses, filling in the critical transition region for temperate planets in the mass–radius–temperature diagram, providing additional constraints on their orbital parameters, and also allowing the detection of additional, non-transiting companions. We are pursuing a followup program with *Spitzer* to refine orbit ephemerides and search for TTVs in small *K2* planets transiting M dwarfs. The transit of K2-26b has been independently detected in this program and the *Spitzer* data provides consistent transit parameters (Beichman et al. 2016). Atmospheric characterization via transmission or emission spectroscopy is infeasible in the near future because both stars are too faint for transit spectroscopy to be practical with the *JWST* (Beichman et al. 2014; Cowan et al. 2015). However, such observations may be feasible with next-generation, ground-based 30 m class telescopes (Cowan et al. 2015).

5. CONCLUSION

We report on two small temperate planets orbiting relatively nearby cool stars observed during the *K2* mission. Our detailed characterizations based on our own observations and other available data reveal K2-26b may have an eccentric orbit. We find that K2-9b lies in the optimistic HZ of its host star but may receive high levels of UV flux that would likely affect the chemistry of its presumed upper atmosphere. Future observations can provide masses for the planets and critical constraints on the transition between rocky and volatile rich bodies. The *Kepler* spacecraft continues its legacy of discovery and is expected to observe many more fields around the ecliptic during its *K2* mission to reveal more small planets orbiting low-mass stars.

Facilities: Kepler, *K2*, IRTF (SpeX), NTT (EFOSC2), LBT (LBTI/LMIRcam), Keck:I (HIRES), Keck:II (NIRC2), PO:1.5 m (Robo-AO), PO:5.0 m (Double Spectrograph).

REFERENCES

Abazajian, K. N., Adelman-McCarthy, J. K., Agüeros, M. A., et al. 2009, ApJS, 182, 543
Abell, G. O. 1955, PASP, 67, 258
Abell, G. O. 1966, ApJ, 144, 259
Agol, E., Steffen, J., Sari, R., & Clarkson, W. 2005, MNRAS, 359, 567
Akeson, R. L., Chen, X., Ciardi, D., et al. 2013, PASP, 125, 989
Artigau, É., Kouach, D., Donati, J.-F., et al. 2014, Proc. SPIE, 9147, 15
Bailey, V. P., Hinz, P. M., Puglisi, A. T., et al. 2014, Proc. SPIE, 9148, 03
Baraffe, I., Homeier, D., Allard, F., & Chabrier, G. 2015, A&A, 577, A42
Baranec, C., Riddle, R., Law, N. M., et al. 2013, JVE, 72, e50021
Baranec, C., Riddle, R., Law, N. M., et al. 2014, ApJL, 790, L8
Barnes, R., Raymond, S. N., Jackson, B., & Greenberg, R. 2008, AsBio, 8, 557
Batalha, N., Kalirai, J., Lunine, J., Clampin, M., & Lindler, D. 2015, arXiv:1507.02655
Bean, J. L., Désert, J.-M., Kabath, P., et al. 2011, ApJ, 743, 92
Becker, J. C., Vanderburg, A., Adams, F. C., Rappaport, S. A., & Schwengeler, H. M. 2015, ApJL, 812, L18
Beichman, C., Benneke, B., Knutson, H., et al. 2014, PASP, 126, 1134
Beichman, C. A., et al. 2016, ApJ, submitted
Bensby, T., & Feltzing, S. 2010, in IAU Symp. 265, Chemical Abundances in the Universe: Connecting First Stars to Planets, ed. K. Cunha, M. Spite, & B. Barbuy (Cambridge: Cambridge Univ. Press), 300
Bochanski, J. J., Hawley, S. L., Covey, K. R., et al. 2010, AJ, 139, 2679
Bohlin, R. C., Dickinson, M. E., & Calzetti, D. 2001, AJ, 122, 2118
Boyajian, T. S., von Braun, K., van Belle, G., et al. 2012, ApJ, 757, 112
Brandt, T. D., & Huang, C. X. 2015a, ApJ, 807, 58
Brandt, T. D., & Huang, C. X. 2015b, ApJ, 807, 24

Bryson, S. T., Jenkins, J. M., Gilliland, R. L., et al. 2013, PASP, 125, 889
Buzzoni, B., Delabre, B., Dekker, H., et al. 1984, Msngr, 38, 9
Charbonneau, D., Berta, Z. K., Irwin, J., et al. 2009, Natur, 462, 891
Claret, A., Hauschildt, P. H., & Witte, S. 2012, A&A, 546, A14
Cowan, N. B., Greene, T., Angerhausen, D., et al. 2015, PASP, 127, 311
Crossfield, I. J. M., Petigura, E., Schlieder, J. E., et al. 2015, ApJ, 804, 10
Cushing, M. C., Rayner, J. T., & Vacca, W. D. 2005, ApJ, 623, 1115
Cushing, M. C., Vacca, W. D., & Rayner, J. T. 2004, PASP, 116, 362
Cutri, R. M., Skrutskie, M. F., van Dyk, S., et al. 2003, The IRSA 2MASS All-Sky Point Source Catalog, NASA/IPAC Infrared Science Archive
Cutri, R. M., Wright, E. L., Conrow, T., et al. 2013, yCat, 2328, 0
Dawson, R. I., & Johnson, J. A. 2012, ApJ, 756, 122
Dressing, C. D., & Charbonneau, D. 2013, ApJ, 767, 95
Dressing, C. D., & Charbonneau, D. 2015, ApJ, 807, 45
Espinoza, N., & Jordán, A. 2015, MNRAS, 450, 1879
Esposito, S., Riccardi, A., Pinna, E., et al. 2011, Proc. SPIE, 8149, 814902
Esposito, S., Riccardi, A., Quirós-Pacheco, F., et al. 2010, ApOpt, 49, G174
Foreman-Mackey, D., Hogg, D. W., Lang, D., & Goodman, J. 2013, PASP, 125, 306
France, K., Froning, C. S., Linsky, J. L., et al. 2013, ApJ, 763, 149
Gizis, J. E. 1997, AJ, 113, 806
Gunn, J. E., Siegmund, W. A., Mannery, E. J., et al. 2006, AJ, 131, 2332
Hamuy, M., Suntzeff, N. B., Heathcote, S. R., et al. 1994, PASP, 106, 566
Henden, A. A., Levine, S. E., Terrell, D., Smith, T. C., & Welch, D. 2012, JAVSO, 40, 430
Hinz, P. M., Bippert-Plymate, T., Breuninger, A., et al. 2008, Proc. SPIE, 7013, 28
Hirano, T., Fukui, A., Mann, A. W., et al. 2015, ApJ, submitted (arXiv:1511.08508)
Holman, M. J., & Murray, N. W. 2005, Sci, 307, 1288
Howard, A. W., Marcy, G. W., Bryson, S. T., et al. 2012, ApJS, 201, 15
Howell, S. B., Sobeck, C., Haas, M., et al. 2014, PASP, 126, 398
Jackson, B., Barnes, R., & Greenberg, R. 2008a, MNRAS, 391, 237
Jackson, B., Greenberg, R., & Barnes, R. 2008b, ApJ, 678, 1396
Johnson, D. R. H., & Soderblom, D. R. 1987, AJ, 93, 864
Jones, D. O., & West, A. A. 2016, ApJ, 817, 1
Kasting, J. F., Whitmire, D. P., & Reynolds, R. T. 1993, Icar, 101, 108
Kirkpatrick, J. D., Henry, T. J., & McCarthy, D. W., Jr. 1991, ApJS, 77, 417
Kolbl, R., Marcy, G. W., Isaacson, H., & Howard, A. W. 2015, AJ, 149, 18
Kopparapu, R. K., Ramirez, R., Kasting, J. F., et al. 2013, ApJ, 765, 131
Kopparapu, R. K., Ramirez, R. M., SchottelKotte, J., et al. 2014, ApJL, 787, L29
Kotani, T., Tamura, M., Suto, H., et al. 2014, Proc. SPIE, 9147, 14
Kraus, A. L., & Hillenbrand, L. A. 2007, AJ, 134, 2340
Kreidberg, L. 2015, PASP, 127, 1161
Kreidberg, L., Bean, J. L., Désert, J.-M., et al. 2014, Natur, 505, 69
Law, N. M., Morton, T., Baranec, C., et al. 2014, ApJ, 791, 35
Lawson, W. A., Lyo, A.-R., & Bessell, M. S. 2009, MNRAS, 400, L29
Leisenring, J. M., Skrutskie, M. F., Hinz, P. M., et al. 2012, Proc. SPIE, 8446, 84464F
Lépine, S., & Gaidos, E. 2011, AJ, 142, 138
Lépine, S., Hilton, E. J., Mann, A. W., et al. 2013, AJ, 145, 102
Lépine, S., & Shara, M. M. 2005, AJ, 129, 1483
Linsky, J. L., France, K., & Ayres, T. 2013, ApJ, 766, 69
Luger, R., & Barnes, R. 2015, AsBio, 15, 119
Lyo, A.-R., Lawson, W. A., & Bessell, M. S. 2004, MNRAS, 355, 363
Mahadevan, S., Ramsey, L. W., Terrien, R., et al. 2014, Proc. SPIE, 9147, 1
Maire, A.-L., Skemer, A. J., Hinz, P. M., et al. 2015, A&A, 576, A133
Maldonado, J., Affer, L., Micela, G., et al. 2015, A&A, 577, A132
Mandel, K., & Agol, E. 2002, ApJL, 580, L171
Mann, A. W., Gaidos, E., & Ansdell, M. 2013a, ApJ, 779, 188
Mann, A. W., Gaidos, E., Kraus, A., & Hilton, E. J. 2013b, ApJ, 770, 43
Marcy, G. W., Butler, R. P., Vogt, S. S., et al. 2008, PhST, 130, 014001
Marcy, G. W., Isaacson, H., Howard, A. W., et al. 2014, ApJS, 210, 20

Martin, D. C., Fanson, J., Schiminovich, D., et al. 2005, ApJL, 619, L1
Miguel, Y., Kaltenegger, L., Linsky, J. L., & Rugheimer, S. 2015, MNRAS, 446, 345
Minkowski, R. L., & Abell, G. O. 1963, in The National Geographic Society-Palomar Observatory Sky Survey, ed. K. A. Strand (Chicage, IL: Univ. Chicago Press), 481
Montet, B. T., Morton, T. D., Foreman-Mackey, D., et al. 2015, ApJ, 809, 25
Morton, T. D. 2012, ApJ, 761, 6
Morton, T. D. 2015, Astrophysics Source Code Library, ascl:1503.011
Oke, J. B., & Gunn, J. E. 1982, PASP, 94, 586
Parviainen, H. 2015, ascl soft, ascl:1510.003
Parviainen, H., & Aigrain, S. 2015, MNRAS, 453, 3821
Pecaut, M. J., & Mamajek, E. E. 2013, ApJS, 208, 9
Perryman, M. A. C., Brown, A. G. A., Lebreton, Y., et al. 1998, A&A, 331, 81
Petigura, E. A., Howard, A. W., & Marcy, G. W. 2013a, PNAS, 110, 19273
Petigura, E. A., & Marcy, G. W. 2012, PASP, 124, 1073
Petigura, E. A., Marcy, G. W., & Howard, A. W. 2013b, ApJ, 770, 69
Petigura, E. A., Schlieder, J. E., Crossfield, I. J. M., et al. 2015, ApJ, 811, 102
Quirrenbach, A., Amado, P. J., Caballero, J. A., et al. 2014, Proc. SPIE, 9147, 1
Rasio, F. A., Tout, C. A., Lubow, S. H., & Livio, M. 1996, ApJ, 470, 1187
Rayner, J. T., Cushing, M. C., & Vacca, W. D. 2009, ApJS, 185, 289
Rayner, J. T., Toomey, D. W., Onaka, P. M., et al. 2003, PASP, 115, 362
Reid, I. N., Brewer, C., Brucato, R. J., et al. 1991, PASP, 103, 661
Reid, I. N., Hawley, S. L., & Gizis, J. E. 1995, AJ, 110, 1838
Riccardi, A., Xompero, M., Briguglio, R., et al. 2010, Proc. SPIE, 7736, 2
Ricker, G. R., Winn, J. N., Vanderspek, R., et al. 2014, Proc. SPIE, 9143, 20
Roeser, S., Demleitner, M., & Schilbach, E. 2010, AJ, 139, 2440
Rogers, L. A. 2015, ApJ, 801, 41
Rojas-Ayala, B., Covey, K. R., Muirhead, P. S., & Lloyd, J. P. 2012, ApJ, 748, 93
Schlieder, J. E., Lépine, S., Rice, E., et al. 2012a, AJ, 143, 114
Schlieder, J. E., Lépine, S., & Simon, M. 2012b, AJ, 143, 80
Segura, A., Walkowicz, L. M., Meadows, V., Kasting, J., & Hawley, S. 2010, AsBio, 10, 751
Shkolnik, E. L., & Barman, T. S. 2014, AJ, 148, 64
Shkolnik, E. L., Liu, M. C., Reid, I. N., Dupuy, T., & Weinberger, A. J. 2011, ApJ, 727, 6
Shkolnik, E. L., Rolph, K. A., Peacock, S., & Barman, T. S. 2014, ApJL, 796, L20
Skrutskie, M. F., Jones, T., Hinz, P., et al. 2010, Proc. SPIE, 7735, 77353H
Southworth, J. 2011, MNRAS, 417, 2166
Southworth, J., Maxted, P. F. L., & Smalley, B. 2004, MNRAS, 349, 547
Stelzer, B., Marino, A., Micela, G., López-Santiago, J., & Liefke, C. 2013, MNRAS, 431, 2063
Terrien, R. C., Mahadevan, S., Bender, C. F., et al. 2012, ApJL, 747, L38
Vacca, W. D., Cushing, M. C., & Rayner, J. T. 2003, PASP, 115, 389
van Dam, M. A., Bouchez, A. H., Le Mignant, D., et al. 2006, PASP, 118, 310
Vanderburg, A. 2014, arXiv:1412.1827
Vanderburg, A., Latham, D. W., Buchhave, L. A., et al. 2016, ApJS, 222, 14
Vanderburg, A., Montet, B. T., Johnson, J. A., et al. 2015, ApJ, 800, 59
Vogt, S. S., Allen, S. L., Bigelow, B. C., et al. 1994, Proc. SPIE, 2198, 362
Weiss, L. M., & Marcy, G. W. 2014, ApJL, 783, L6
Welsh, B. Y., Wheatley, J. M., Seibert, M., et al. 2007, ApJS, 173, 673
West, A. A., Hawley, S. L., Bochanski, J. J., et al. 2008, AJ, 135, 785
West, A. A., Morgan, D. P., Bochanski, J. J., et al. 2011, AJ, 141, 97
Wizinowich, P. L., Le Mignant, D., Bouchez, A. H., et al. 2006, PASP, 118, 297
Wolfgang, A., & Lopez, E. 2015, ApJ, 806, 183
Wolfgang, A., Rogers, L. A., & Ford, E. B. 2015, ApJ, submitted (arXiv:1504.07557)
York, D. G., Adelman, J., Anderson, J. E., Jr., et al. 2000, AJ, 120, 1579